HELLENIC REPUBLIC
National and Kapodistrian University of Athens
EST. 1837

School of Medicine and Department of Pharmacy

New conjugated polymer NPs for bio-imaging

Interdisciplinary Postgraduate Studies Program in

Nanomedicine

Master Thesis

Lida Evmorfia Vagiaki

Supervisor: Associate Prof. Dionysios E. Mouzakis

Co-supervisor: Dr. Christos Chochos, NHRF, Institute of Chemical Biology

Three Member Committee:

Prof. Efstathopoulos Efstathios

Associate Prof. Gazouli Maria

Associate Prof. Dionysios E. Mouzakis

ATHENS

August 2019

Abstract

Conjugated polymers (CPs) are a special category of macromolecules with large π-conjugated backbones. Owing to their highly electron-delocalized structures and efficient coupling between optoelectronic segments, CPs absorb and emit light energy in the UV-Vis and the NIR region, which can be effectively converted to photoacoustic and fluorescence effects [1]. Nevertheless, for biological applications it is imperative that the CPs are water-soluble. Since CPs are generally hydrophobic, we implemented strategies to enable solubility in aqueous media. Therefore, low-bandgap aqueous conjugated polymer nanoparticles (CPNs) have been successfully prepared and thoroughly applied in biological applications and especially in bio-imaging, due to their unique optoelectronic properties [2],[3]. Specifically, CPNs attracted wide attention since they exhibit excellent properties such as high fluorescence, excellent photostability, high signal-to-noise ratio, high emission rates, and low cytotoxicity [3]-[5]. Moreover, the absorbance in the UV-VIS and the NIR region, which is called the biological window, allows deep tissue penetration, critical for medical applications such as imaging.

Scope

In this study, we examine the potential use of novel low bandgap water soluble conjugated polymers dots as fluorescent contrast agents. Under this scope, we synthesized one series of CPs which consists of thiadiazoloquinoxaline biphenyl substituted-bithiophene and thiadiazoloquinoxaline bimethyl substituted-bithiophene, BTTDQ-Ph and BTTDQ-Me, respectively.

Acknowledgement

This thesis was performed from February 2019 until August 2019 at the National Hellenic Research Foundation, Institute of Biology, Medicinal Chemistry & Biotechnology in Athens.

I would like to express my deep and sincerest gratitude to Prof. Mouzaki, for giving me the opportunity to work in Christos Chochos' group on the very interesting field of conjugated polymer NPs that absorb and emit light energy in the UV-Vis and the NIR region, which can be effectively converted to photoacoustic and fluorescence effects for therapy and diagnosis of several cancer types. I would also like to thank Dr. Chochos, my research supervisor, for the patient guidance, encouragement, confidence and trust that he has placed in me throughout this master thesis. His guidance, educational skills and unlimited motivation were indispensable for the completion of my thesis. Also, for this project I was very fortunate to have collaborations with very dedicated partners; Dr. Alkmini Negka and Dr. Panagiota Koralli from the German Cancer Research Center, Cinical Cooperation Unit Nuclear Medicine located in Heidelberg, Germany. Their support and valuable advice throughout this thesis were very important to me. It is beyond question, that this research project is a contribution of the whole research group of Dr. Chochos.

It would be impossible not to thank Prof. Xenaki and his research group for their excellent technical assistance with the Dynamic Light Scattering (DLS). Additionally, the contribution of Prof. Zoumpourli and his research group was crucial for the cytotoxicty assays, as well.

I would finally like to express my gratitude towards my family for their support during this thesis, and encouragement in every educational and scientific step that I have made, and my friends for their support and patience.

Table of Contents

List of Figures

Figure **Page**

List of Tables **Page**

1. Introduction

1.1 Types of cancer and statistics

Cancer is the world's second-largest cause of death, with an estimated 9.6 million fatalities in 2018 [6],[7]. Overall, a malignant tumor causes about 1 in 6 fatalities. In low- and middle-income nations, about 70 percent of cancer fatalities happen. Approximately one third of cancer fatalities are due to the five major behavioral and nutritional hazards: elevated body mass index, low intake of fruit and vegetables, absence of physical activity, use of tobacco, and use of alcohol. In particular, cancer is caused by the conversion of ordinary cells into tumor cells in a multi-stage process that usually develops from a pre-cancerous lesion to a malignant tumor[8]. These mutations are the result of the interaction between a person's genetic factors and 3 categories of external agents, including:

i. physical carcinogens, such as ultraviolet and ionizing radiation;

ii. chemical carcinogens, such as asbestos, components of tobacco smoke, aflatoxin (a food contaminant), and arsenic (a drinking water contaminant); and

iii. biological carcinogens, such as infections from certain viruses, bacteria, or parasites.

Moreover, according to new cancer statistics, a total of 1,762,450 new cancer cases and 606,880 deaths from cancer are expected to occur in the US in 2019 [9].

The most common tumor types diagnosed in men are prostate, lung, and colorectal cancers. Together, they account for 42% of all cases in men, with prostate cancer alone accounting for nearly 1 in 5 new cases. For women, the 3 most common cancers are breast, lung, and colorectal. Together, they account for one-half of all cases, with breast cancer alone accounting for 30% of new cases. Among children ages 1 to 14 years, cancer is the second most common cause of death after car accidents [10]. In 2019, an estimated number of 11,060 children in this age group will be diagnosed with cancer and 1,190 will die from it. Leukemia accounts for almost a third (28%) of all childhood cancers, followed by brain and other nervous system tumors (26%). The risk of cancer rises with age, most probable

owing to increased hazards for particular cancers that increase with age and the quickly increasing elderly population will boost the demand for care for cancer. The overall risk accumulation is combined with the tendency for cellular repair mechanisms to be less effective as a person grows older [11].

The early diagnosis and detection of a malignant tumor is of great importance, since it is more likely to be treated successfully. Taken in time and when in an accessible position, before metastasis occurs, the odds of survival are high. The aim is the recognition of a malignant tumor at a stage so early, when it isn't too large and hasn't spread to distant structures. If cancer spreads, effective treatment becomes more difficult, and generally a person's chances of surviving are much lower [12].

1.2 Standard (Pre)Clinical Imaging Modalities

Cancer may be difficult to detect, but for some types of cancer, the earlier it is detected, the better are the chances of treating it effectively. Imaging techniques — methods of producing pictures of the body — have become an important element of early pre-clinical detection of many cancers. But imaging is not simply used for detection. Imaging is also essential to determine the phase (telling how advanced the cancer is) and cancer's accurate location to help the guidance of the surgery and other cancer treatments, or to verify whether a cancer has reoccurred. There are many different types of imaging in order to achieve the optimal visualization of the tumor, regarding the detection limit of each technique. Many features of the neoplastic process [13] can be visualized using molecular imaging [14], including changes in gene expression, the expression of cell surface receptors, changes in epithelial–stromal communication (e.g., signaling associated with epithelial migration and invasion) [15] and epithelial cell apoptosis.

Contrast Agents:

Usually, Standard (Pre)Clinical Imaging Modalities use low doses of radioactive substances linked to compounds used by the body's cells or compounds that attach to tumor cells. Using a particular detection equipment, the radioactive substances can be traced in the

body to see where and when they concentrate. The mentioned- above substances are defined as *contrast agents*.

I. X-Ray Imaging:

Perhaps the most familiar form of imaging is X-ray imaging. Most adults had an X-ray in their chest to look for an infection or perhaps just as part of a health check for jobs. Pictures generated by X-rays are due to distinct tissue absorption rates. The pathological tissues are identified from the surrounding healthy tissues, based upon their different densities and the resulting X-ray absorption variations. Calcium in bones absorbs X-rays the most, so bones look white on a film recording of the X-ray image, called a radiograph. Fat and other soft tissues absorb less, and look gray. Air absorbs least, so lungs look black on a radiograph. The most familiar use of X-rays is checking for broken bones. We can also use X-rays to look for tumors, so X-rays are also used in cancer diagnosis. For example, chest radiographs and mammograms are often used for early cancer detection or to see if cancer has spread to the lungs or other areas in the chest. Mammograms use X-rays to look for tumors or suspicious areas in the breasts. X-ray imaging is considered the most commonly used medical imaging modality, since it is relatively faster and less costly as compared with MRI and PET. To enhance the contrast between normal and anomalous tissues during CT scanning, CT contrast agents, mostly iodine or barium based, are administered to patients before imaging, thereby improving the image resolution and specificity.

II. Ultrasound:

Ultrasound (US) uses sound waves with frequencies above those humans can hear. A transducer sends sound waves traveling into the body which are reflected back from organs and tissues, allowing a picture to be made of the internal organs. Ultrasound may indicate tumors and may also guide physicians who do biopsies. In addition, there is no harmful US diagnostic radiation. Unfortunately, while US is very helpful to image certain components of the body, it is not as helpful as other imaging methods to look at the brain or lungs, for instance.

III. CT Scans:

A computed tomography scan (CT scan, also called a CAT scan) uses computer-controlled X-rays to create images of the body. However, a radiograph and a CT scan show different types of information. Although an experienced radiologist can get a sense for the approximate three-dimensional location of a tumor from a radiograph, in general, a plain radiograph is two-dimensional.

An arm or chest radiograph looks all the way through a body without being able to tell how deep anything is. A CT scan is three-dimensional. By looking at several images of a body's three-dimensional slices, a doctor could not only say if there is a tumor, but how deep it is in the body. A CT scan can be three dimensional because the information about how much of the X-rays are passing through a body is collected not just on a flat piece of film, but on a computer. The data from a CT scan can be enhanced to be more vivid than a plain radiograph. For both plain radiographs and CT scans, the patient may be given a contrast agent to drink and/or by injection to more clearly show the boundaries between organs or between organs and tumors. Conventional CT scans take pictures of slices of the body (like slices of bread). These slices are a few millimeters apart. The newer spiral (also called helical) CT scan takes continuous pictures of the body in a rapid spiral motion, so that there are no gaps in the pictures collected.

IV. Magnetic Resonance Imaging (MRI):

MRI uses strong magnetic field to align the nuclear spins and generates images from emitted radio frequency (RF) from the nuclei when they return to their original states [16],[17]. ^{1}H signals from water molecules are most frequently visualized. MRI generates high-resolution images (up to single-cell resolution) of soft tissues such as: i) muscles, ii) joints and iii) brain. Abnormalities of tissues appear as darker (T1-weighted) or brighter (T2-weighted) than healthy tissues, due to differences in relaxation times.

Different tissues (including tumors) emit a more or less intense signal based on their

chemical makeup, so a picture of the body organs can be displayed on a computer screen. Much like CT scans, MRI can produce three-dimensional images of sections of the body, but MRI is sometimes more sensitive than CT scans for distinguishing soft tissues. The contrast agents that are clinically used in MRI are: i) paramagnetic gadolinium (Gd) reagents, ii) superparamagnetic iron oxide nanoparticles (SPIONs) and iii) manganese-based reagents. One of the limitations of MRI imaging is the relatively long acquisition times required to obtain high-quality images, where patients are uncomfortable and restrained. Moreover, it would be a misstep not to mention that there are limited applications of MRI for patients with implanted metal devices because the metal could interfere with imaging, and malfunction of the implanted metal device is possible during MRI acquisition within the high magnetic field instrumentation [18].

In an overview, CT and MRI generate high-resolution images, but they basically provide morphological information.

V. PET Scan:

The positron emission tomography (PET) scan generates computerized pictures of chemical changes occurring in tissue, such as sugar metabolism. Typically, a substance consisting of a mixture of a sugar and a tiny quantity of radioactively marked sugar is injected into the patient. The radioactive sugar can help in locating a tumor, because cancer cells take up or absorb sugar more avidly than other tissues in the body [17]. Commonly used tracers for PET are: ^{18}F, ^{13}N, ^{11}C, ^{15}O, ^{82}Rb, ^{68}Ga, and ^{64}Cu. After receiving the radioactive sugar, the patient lies still for about 60 minutes while the radioactively labeled sugar circulates throughout the body. If a tumor is present, the radioactive sugar will accumulate in the tumor. The patient then lies on a table, which gradually moves through the PET scanner incrementally several times during a 15-60-minute period. The PET scanner is used to detect the distribution of the sugar in the tumor and in the body. By the combined matching of a CT scan with PET images, there is an improved capacity to discriminate normal from abnormal tissues. A computer translates this information into the images that are interpreted by a radiologist.

PET scans can be used to determine if a mass is cancerous. PET scans, however, are more

precise in identifying bigger and more aggressive tumors than in finding tumors that are less than 8 mm and/or less aggressive. When other imaging methods demonstrate ordinary outcomes, PET scan may also detect cancer. Moreover, PET scans may be helpful in evaluating and staging recurrent disease (cancer that has come back) and are also commonly used to check if a treatment is working.

VI. SPECT Scan:

Similar to PET, single photon emission computed tomography (SPECT) uses radioactive tracers and a scanner to record data that a computer constructs into two- or three-dimensional images. Commonly used tracers for SPECT are: ^{67}Ga, ^{99}mTc, and ^{111}In. A small amount of a radioactive drug is injected into a vein and a scanner is used to make detailed images of areas inside the body where the radioactive material is taken up by the cells. SPECT can give information about blood flow to tissues and chemical reactions (metabolism) in the body.

In this procedure, antibodies (proteins that recognize and stick to tumor cells) can be linked to a radioactive substance. If a tumor is present, the antibodies will stick to it. Then a SPECT scan can be done to detect the radioactive substance and reveal where the tumor is located.

In an overview, the γ-rays are collected by detectors surrounding the patient in PET or rotating around the patient in SPECT. PET is highly sensitive and quantitative, as compared to SPECT. Moreover, PET requires only 10^{-11}-10^{-12} M radioactive tracers, while SPECT requires 10^{-10}-10^{-11} M. One of the main disadvantages of radioactive tracers (RTs) is their lifetime. The RTs decay much faster than image-acquisition times. The development of tracers that have lifetimes that coincide with the time periods required for sample preparation, purification, distribution to remote imaging facilities, and completion of stable imaging, would be beneficial.

PET/SPECT and MRI have shown promise for imaging of cancer [18]. Specifically, 2-deoxy-2-^{18}F-fluoro-d-glucose PET imaging is now used routinely to assess the response of solid tumors to therapy. However, PET/SPECT and MRI are too expensive for population-based screening [7], and as long as PET/SPECT imaging is concerned, it requires intravenous (iv.)

injection of contrast agent, which is impractical in low-risk populations.

1.3 Nanoparticles

The nano-scale materials (10^{-9} m) present many advantages such as high surface-area- to-volume ratio, high electrical conductivity, magnetic properties, and unique physiochemical properties due to their small size. These properties make them have numerous uses.

Nanomaterial's superior properties and nanofabrication technologies are constantly being exploited in order to design novel nanomaterials. The small dimensions, higher surface area, improved solubility and multifunctionality of nanoparticles, made them ideal for further research in different scientific fields. In particularly, NPs have many special properties regarding the particle aggregation, photoemission, electrical, magnetic, luminescent, heat conductivity and catalytic activity. In previous studies the usage of NPs has been reported in numerous biological applications such as contrast agents in bioimaging, bio-molecule detection, sample separation, signal transduction and amplification [19]. Additionally NPs' selectivity, biocompatibility, non-toxicity, reversibility, rapid response and sensitivity enhanced the signal transduction technologies. The most commonly used nanoparticles in bio-imaging applications are i) metallic NPs (i.e. GNPs which according to their size provide distinguish colors), ii) carbon nanotubes (CNTs), iii) polymer nanoparticles (NPs) and iv) quantum dots (which are nanoscale semiconductor devices), because of their high sensitivity and specificity of detecting materials' physical, chemical, physicochemical, mechanical, optic and magnetic features. This light effect excides particles from the surface as ionic species. Thus, nanoparticles receive photonic properties and they can be used as fluorophores agents [20].

1.4 Optical Clinical Imaging Modalities

It is beyond doubt, that the pre-clinical imaging plays a crucial role for the detection and early diagnosis of a malignant tumor. However, it is not that practical for the clinicians. It is quite common, that even after the surgical removal of the tumor, the patient undergoes a series of therapies such as chemotherapy and radiotherapy, in case of any remaining cancer cells. It would be a great benefit to relocate the imaging from the pre-clinical stage, to the real time – clinical stage during the surgery. This way, the clinician would be assured, about the limits of the cancerous and healthy tissues. The Noninvasive Medical Imaging includes the use of portable set ups such as the Fluoresence and Photoacoustic Imaging (PA).

Up to now, the most widely developed Fluorescence/PA agents are inorganic nanomaterials such as noble metal nanomaterials (e.g., Au and Pd), transition metal dichalcogenides (e.g., MoS_2, WS_2 nanosheets, and CuS_2 nanoparticles), and carbon nanomaterials (e.g., graphene and carbon nanotubes). However, a potential concern is that these typical non-biodegradable inorganic nanomaterials could remain in the body for a long period of time, which could lead to potential long-term biotoxicity and significantly hindering potential *in vivo* applications. Subsequently, the development of organic nanomaterials for clinical imaging is of great demand. PA imaging is not within the scope of this project but it is important to mention that it is considered as a quite promising technique even though currently, there are no organic probes for the PA imaging in the market.

1.5 Conjugated Polymers

Since the conferring of the Nobel Prize in Chemistry to conducting polymers in 2000, the versatile class of polymeric materials has generated tremendous interest from academia and industry. Conjugated polymers are organic macromolecules with π-conjugated backbone, which could be designed to display high electrical conductivity, outstanding

photophysical properties and excellent biocompatibility. They have been extensively explored for a wide range of applications, spanning electronics and energy harvesting to nanobiotechnology and especially in nanomedicine. While the last years have witnessed their rapid development in optoelectronic devices, the emerging field of conjugated polymers for biomedical applications has simultaneously attracted increasing attention recently. Specifically, they have found innovative applications in a variety of biotechnologies, ranging from biosensing that takes advantage of optical amplification, to cell imaging and image-guided therapy that fully utilizes the light-harvesting properties of conjugated polymers. In fact, with their unique biophysicochemical attributes, conjugated polymer nanoparticles have been demonstrated to be even superior to other classes of nanomaterials, such as small organic dye-nanomolecules, semiconducting quantom dots, and inorganic nanoparticles in many biomedical applications.

Conjugated polymer dots are considered one of the upcoming contrast agents for bioimaging. Conjugated polymers where initially used in photo-voltaics as dielectrics. They exhibit conductive, piezoelectric or pyroelectric properties, nonlinear optical properties, and if stimulated, they emit light. By the term conjugated polymer we describe a polymer with altering single and double bonds in the polymer chain. Due to their chains, conjugated polymers have the ability of electron delocalization and subsequent charge-movement around the whole system. This specific property makes them conductive. Specifically, when electrons are removed from the backbone they act as anions [21],[22].

In order to understand the properties of an organic semiconductor we will use as an example the C-C bond. The electron configuration of carbon is $1s^2 2s^2 2p^{2.}$. Carbon has four electrons in its valence shell (outershell) and two core electrons ($1s^2$). Atomic orbitals with s-character have spherical symmetry and a representation of the surface of the carbon 1s orbital is shown in Fig. 1a.

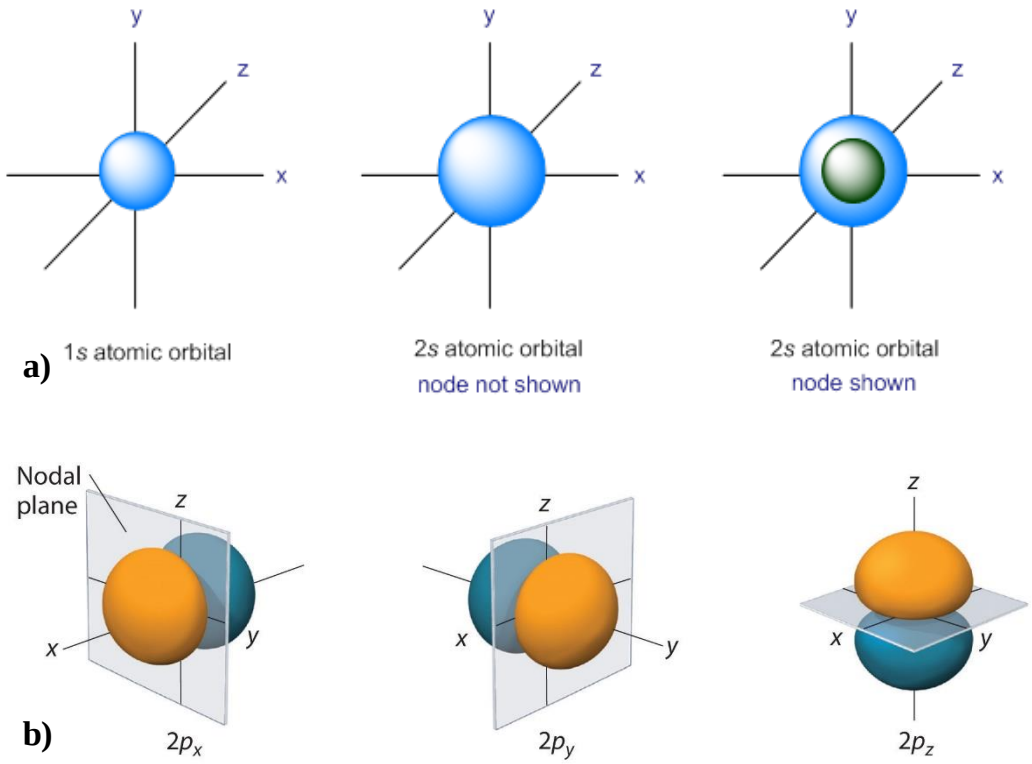

Fig.1(a,b) A representation of the surface of the carbon 1s and 2s orbitals.

The wave properties of electrons make the description of the 2s orbital slightly more complex than the corresponding 1s orbital, in that, within the 2s sphere there is a region in which the amplitude of the electron standing wave falls to zero, that is, there is zero probability of finding the electron in this node region. Nodes are most easily seen in the description of the 2p atomic orbitals, which are shown in Fig. 1b.

The electron densities along the x, y and z axes of the 2p orbitals are clearly shown in the figure; the nodes are the points at the origin and at these points, there is zero probability of finding the electron [23],[24]. The sharing of electrons in a covalent bond occurs by overlap of the individual atomic orbitals. Head-on overlap between energetically compatible orbitals generates sigma (s) bonds, while sideways overlap (typically from adjacent *p* orbitals) generates pi (p) bonds. Examples of sigma and p-bond bond formation between atoms "A" and "B" are shown below (Fig.2).

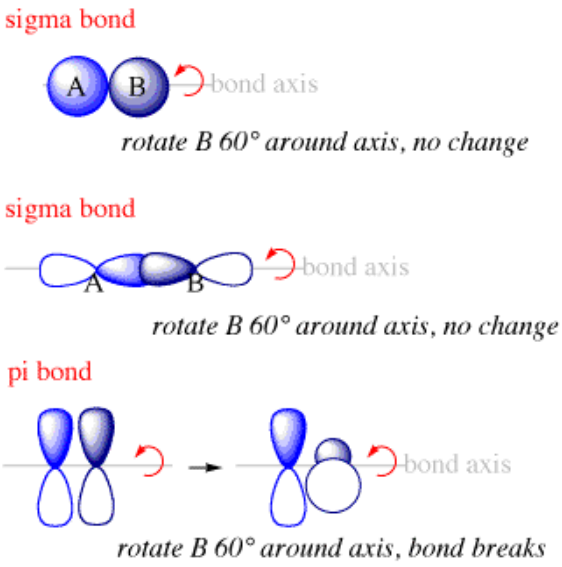

Fig. 2 Examples of sigma and p-bond bond formation between atoms "A" and "B".

The nature of the bonding in carbon (C_2) can be described using Molecular Orbital Theory. As the two atomic orbitals approach each other and begin to overlap, there is a decrease in the net energy of the system because the electrons in each atom tend to become attracted to the positive nucleus of the other atom, as well as their own nucleus. The more the orbitals overlap, the more the energy decreases, until the nuclei approach so closely that they begin to repel each other. The point at which the repulsive and attractive forces balance defines the bond distance for a given covalent bond. In molecular orbital theory, the number of atomic orbitals used to make the covalent bond must equal the total number of molecular orbitals in the molecule. The molecular orbital description of this simple covalent bonding is shown below (Fig.3). As described above, the bonding orbital is referred to as a s/π-orbital, while the corresponding antibonding orbital is referred to as a s*/π*-orbital [25]. Overlapping, according to quantum mechanics can be either "efficient", if the fluctuations are in phase, or "destructive" if the fluctuations are out of phase. Thus, respectively, the bonding molecular orbitals and the antibonding molecular orbitals (AMD) arise.

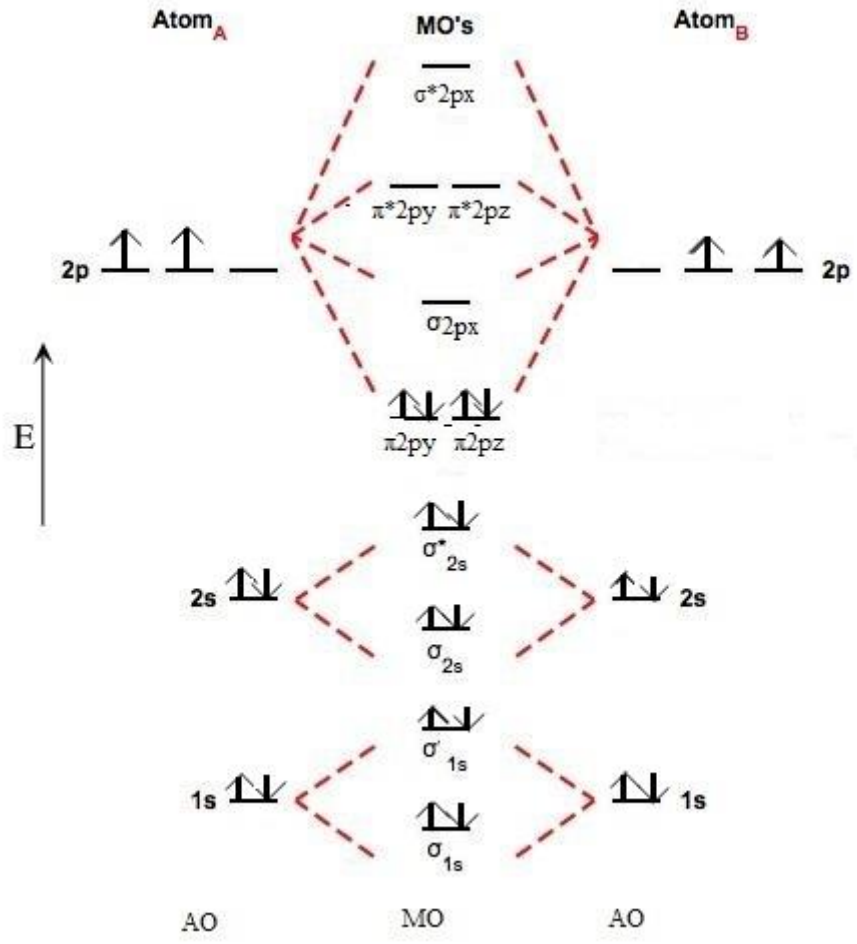

Fig.3 The molecular orbital description of C_2.

Sigma (σ) bonding molecular orbital: Shared electron density is directly between the bonding atoms along the bonding axis. A sigma bond is always the first bond formed between two atoms.

Pi bond (π): bonding molecular orbital: The bonding electron density lies above and below, or in front and in back of the bonding axis, with no electron directly on the bonding axis, since 2p orbitals do not have any electron density at the nucleus.

Sigma star (σ*) and Pi star (π*) antibonding molecular orbital: Normally this orbital is empty, but if it should be occupied, the wave nature of electron density (when present) is

out of phase (destructive interference) and canceling in nature. There is a node between the bonding atoms (zero electron density). This produces repulsion between the two interacting atoms, when electrons are present.

It is important to mention, that the antibonding molecular orbital is also known as the LUMO *(lowest unoccupied molecular orbital)* energy level. Only the HOMO *(highest occupied molecular orbital)* molecular orbital bond is occupied by electrons. The highest energy antibonding molecular orbital (LUMO) is empty [27].

Conjugated polymers is a category of polymers that consists of alternating repeated subunits that form both sigma and pi-bonds [28]. The electric effect that these polymers exhibit is a result of the overlapping of the p_z molecular orbitals (pi conjugation). The extent of overlapping (conjugation length) determines the HOMO-LUMO band gap of these semiconductors (Fig.4).

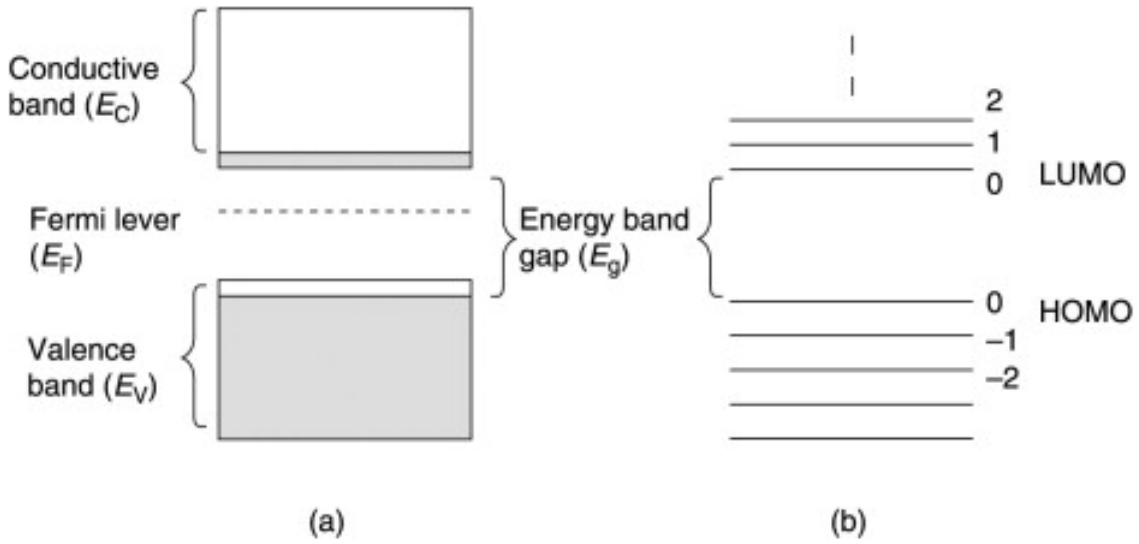

Fig.4 Different HOMO-LUMO band gaps determine the electric conductivity of the polymers.

Conjugated polymers also exhibit a wide range of optical properties which are induced by the addition of impurities that act as electropositive or electronegative. Alterations in the HOMO-LUMO band gap affect the chemical, physical and mechanical characteristics of the conjugated polymers. Generally, the alterations of the HOMO-LUMO band gap are

modified by six factors; i) the molecular weight of the conjugated polymer (CP), ii) the alternation of the bond length, iii) the rotation angle, iv) the aromatic character of the polymer, v) the size of the substituent groups and vi) the intermolecular interactions.

A lot of on-going research focuses on the founding of organic imaging probes that combine high fluorescence, excellent photostability, high brightness, resistance to photo-bleaching, high signal-to-noise ratio, high emission rates, and low cytotoxicity. All these characteristics are ideal for bio-imaging. However, the optical energy gaps of conventional organic materials are normally greater than 2 eV, covering only the visible range of the solar spectrum (300-650 nm). Smaller energy gap organic materials are in demand to extend absorption to the long wavelength region to take advantage of the higher flux, red light and even near infrared region of the solar spectrum. Therefore, it has been a major effort to design and synthesize novel conjugated polymers with narrow energy gaps in recent years [29].

Conjugated polymer nanoparticles (low-bandgap) are considered as a-new-generation contrast agents for bio-imaging, since they are the only organic materials that successfully combine all the mentioned above effects that contribute to new bio-imaging techniques. Thus, CP dots are capable of a wide range of light absorption spectra in the red, far-red and near-infrared regions. Far-red is light at the extreme red end of the visible spectrum, just before infra-red light. Usually, regarded as the region between 710 and 850 nm wavelength.

Table 1: Electromagnetic spectrum in the visible light.

Color:	**Wavelengths (in nm):**
violet	380-450
blue	450-485
cyan	485-500
green	500-565
yellow	565-590
orange	590-625
red	625-740

The near infrared spectroscopy-NIRS, is a spectroscopic method that uses the near-infrared region of the electromagnetic spectrum (from 780 nm to 2500 nm). The father of NIRS, William Herschel, discover it in the 19th century but the first industrial application began in the 1950s. One of the main advantages of the NIR is that it can penetrate much further into the sample than the mid infrared radiation.

According to recent publications [30]-[32], CP dots absorb and emit light energy in the UV-Vis and the NIR region, which can be effectively converted to photoacoustic and fluorescence effects. Novel imaging probes provide an emission spectral window, also known as therapeutic window. The term therapeutic window was introduced, due to the fact that for wavelengths ranging from 650 to 1350 nm, light has its maximum depth of penetration in tissue. Subsequently, we can assume that with the NIR spectrum scientists could probably interfere to the metabolic profile of the cells. The emission spectral window offers i) high tissue penetration, ii) low autofluorescence and also iii) minimization

of various limiting factors including self-absorption and scattering.

Absorptions in the NIR region (780-2500 nm) are generated from fundamental vibrations by two processes; i) overtones, which are harmonics and ii) combinations, which are more complex and the NIR absorptions require more energy than a fundamental absorption. Specifically, combinations arise from the sharing of NIR energy between two or more fundamental absorptions.

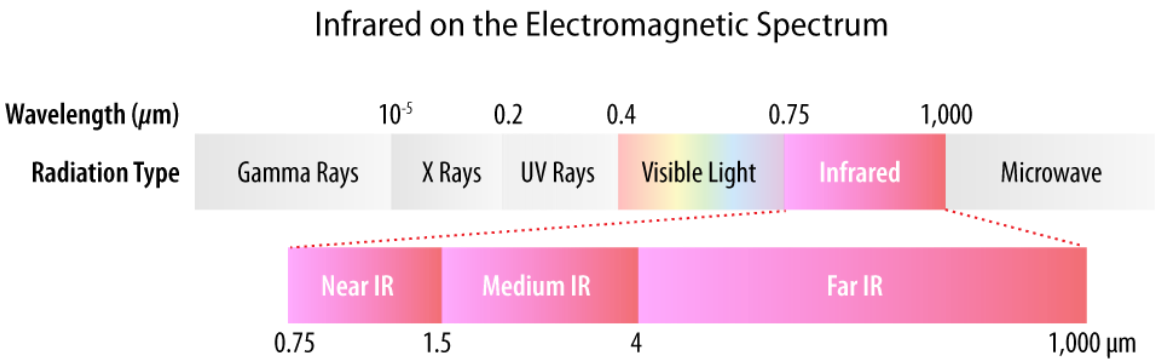

Fig. 5 NIR in the electromagnetic spectrum [33].

Considering the great effects that CP dots possess, many scientific groups attempted to modify their hydrophobic properties recently, in order to use them in the field of bioimaging, signaling and theranostics.

2. Materials and Methods

2.1 Synthesis of Conjugated Polymers

The development of functional polymers is a very active research field and has had huge impact on human society due to their applications in many cutting-edge technologies, such as energy conversion and storage, electronic devices, biotechnology, and health care, to name a few [1]. Scientists from different disciplines have invented numerous new materials for those purposes. Integral to these efforts is the development of efficient, versatile, and scalable synthesis techniques, which in turn enable the development of new functional materials. Thus, new synthetic methodologies are always a critical research topic that is actively pursued. Most recently, polycondensations based on transition metal-catalyzed C-C bond formation reactions have emerged as important methodologies for synthesis of electro -optic materials containing large systems. These reactions include Stille, Suzuki, Negishi, Heck, and so on [34]-[37]. The Stille reaction is one of the versatile methods for the synthesis of organic functional materials due to its stability, excellent compatibility with various functional groups and high reaction yield. The reaction is catalyzed by palladium compounds and carbon-carbon single bonds are formed. The reaction conditions are very mild. Some of the advantages of the Stille reaction is i) that the alkyl groups of Sn are easy to synthesize and to store and ii) that it can be combined with a wide range of functional groups.

The Stille coupling reaction leads to the synthesis of hydrophobic polymers with C-C bond, in the presence of Pd catalyst and the alkyl groups of Sn.

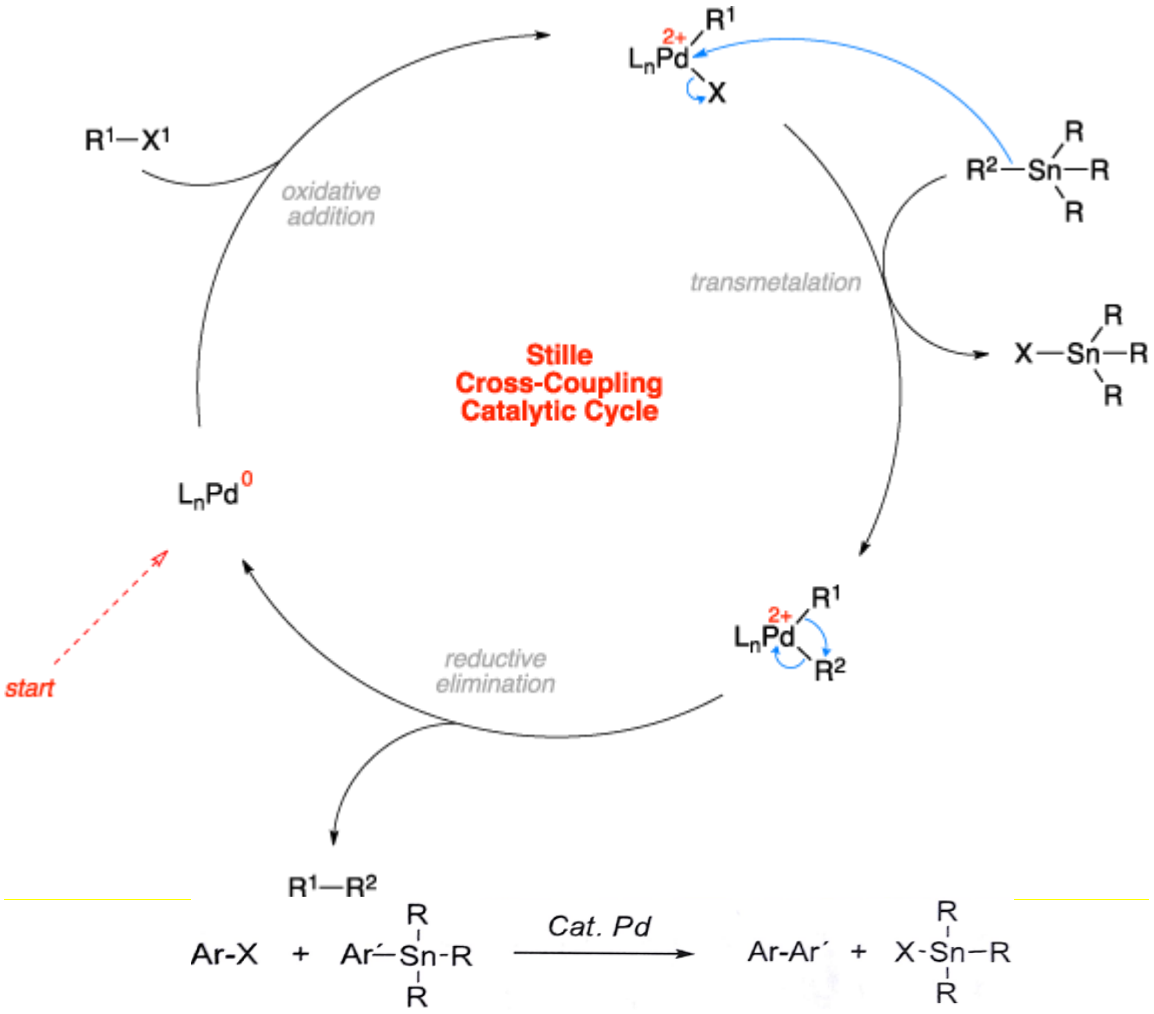

Fig.6 The Stille coupling aromatic reaction.

Analytically, the low-bandgap conjugated polymers were synthesized *via* metal catalyzed aromatic cross coupling Stille polymerization reaction. For the synthesis the monomer 4,9-dibromo-6,7-diphenyl-(1,2,5)thiadiazolo(3,4-g)quinoxaline (SunaTech) and 4,9-dibromo-6,7-dimethyl-(1,2,5)thiadiazolo(3,4-g)quinoxaline (SunaTech) were combined with (4,4'-didodecyl-[2,2'-bithiophene]-5,5'-diyl)bis(trimethylstannane) (SunaTech), to provide BTTDQ-Ph and BTTDQ-Me, respectively. Tris(dibenzylideneacetone)dipalladium(0) (Sigma Aldrich) and tri(o-tolyl)phosphine (Sigma Aldrich) were used as catalyst and ligand and the polymerization took place in anhydrous toluene (Sigma Aldrich). The final polymer was

purified and fractionated *via* sequential Soxhlet extraction with methanol, hexane and chloroform.

2.2 Preparation of Nanoparticles

Conjugated polymers nanoparticles (CPNs) are powerful fluorescent semiconductor materials, which excel through simple fabrication and processing techniques, their great potential for electro- and photoluminescent applications, and their high conductivity as compared to conventional polymers. Furthermore, CPNs shows extraordinary resistance toward photo-oxidation and photo-bleaching and exhibit low cytotoxicity [38]-[41]. The general characteristic of a conjugated molecule can be described as the sequence of altering double (or triple) and single bonds. These alternating double and single bonds generally stabilize a molecule thermodynamically and additionally give the molecule the above characteristics [42]. Besides the easily surface functionalization of CPNs, there are several requirements for CPNs in order to render them suitable for bioimaging and cell tracking applications: (i) the particles should ideally be monodisperse and spherical in shape. Monodisperse particles secure specific labeling of only the targeted type of cell, especially in multicomponent united cell structures. Different cells exhibit different particle uptake kinetics and monodisperse CPNs prevent nonspecific uptake by the non-targeted type of cells [43],[44].

Nanoprecipitation:

In the nanoprecipitation method, a previously synthesized conjugated polymer (CP) is dissolved in a good solvent [45]. This polymer solution is then strongly diluted or added quickly to an excess of a poor solvent (often water). When both solvents are miscible, then the polymer precipitates into small and spherical aggregates. Owing to the rapid increase in polarity upon injection of the polymer solution into the polar solvent (decrease of the solvent hydrophobicity), phase inversion occurs and the polymer chains collapse to form nanoparticles. CPNs are obtained as dispersions in the poor solvent [46]. The size of the

resulting CPNs can be tuned by varying the concentration of the polymer in solution. Ultrasonication is often used to improve mixing of the polymer solution with the poor solvent and further reduce the nanoparticle size. The mechanism of particle stabilization in the resulting dispersion in unclear, since surfactants are often not applied in the preparation of CPNs :[45].

Nanoprecipitation protocol:

1. Each low-bandgap conjugated polymer was dissolved in freshly distilled THF at a concentration of 0.1 mg/mL.

2. A 2-mL portion of this polymer solution was then injected into 10 mL of water under vigorous stirring *via* a tip sonicator which is ideal for nano particle dispersion, mixing and homogenization, resulting in a final concentration of 4 ppm low-bandgap CPdot dispersion.

3. The THF was removed as the samples were left in the hood overnight

4. The suspension was then filtered through a 0.2-µm cellulose acetate filter (Sartorius Stedim Biotech).

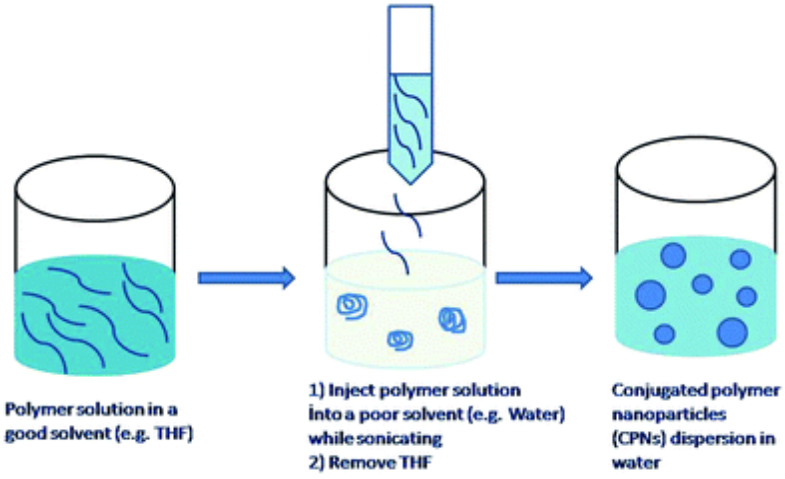

Fig.7 The nanoprecipitation process.

2.3 ^{1}H-NMR

The ^{1}H NMR proton spectrum, which is extensively used to study the stereochemical representation of polymers, consists of a group of spectral lines due to the different proton types of the sample. From one spectrum three basic information is obtained; i)the position of the spectral line or chemical shift, which is characteristic of the type of particles, ii)the area of the area under each spectral line, which is proportional to the number of particles present in the sample and, finally, iii)the range of the spectral line associated with the molecular proton of the particular proton [46].[47].

The coordination of each nucleus at a different frequency is due to the existence of electrons surrounding it. These electrons create local magnetic fields that protect it, causing the core to feel a Bloc field other than the applied B.

$$B_{loc} = B\,(1 - \sigma) \qquad (2.3.1)$$

where σ, (the shielding or screening constant), a dimensionless quantity that determines the electronic density around the core and hence its degree of protection.

The chemical shift of a core is the difference between the core resonance frequency and a standard reference substance. The reference substance for the proton spectrum is tetramethylsilane ($Si(CH_3)_4$), TMS, which has twelve equivalents and highly protected protons. The chemical shift δ is defined by the following equations:

$$\delta = \frac{B_\alpha - B_\delta}{B_\alpha} \times 10^6 ppm \qquad (2.3.2)$$

$$\delta = \frac{v_\alpha - v_\delta}{v_\alpha} \times 10^6 ppm \qquad (2.3.3)$$

where Bα and Bδ are the co-ordinating regions of the reference and sample cores, respectively. Vα and Vδ are the frequencies of the reference substance and the sample, respectively. The more defended a core is (a high value of σ), the resonance will be achieved in highly applied magnetic fields and at a lower frequency. The fact that the area under the spectral line is proportional to the number of particles in the sample is the basis of the quantitative analysis. From the ratio of different spectral lines, which are due to

different kinds of particles, the composition of the copolymers can be determined.

Finally, the degree of peak breaking allows for its identification. The number of spectral lines obtained is 2nxIx + 1, where nx is the number of equivalent neighboring cores and Ix the spin of the kernel. In the case of 1H and 13C, where spin is I = 1/2, the above relation is nx + 1. The relative peak intensities are the coefficients of the terms of the distribution (1 + x) n. A nucleus separated by two other adjacent nuclei, for example, will give a triple peak with 1: 2: 1 peak intensities.

2.4 UV-VIS spectroscopy

Optical spectroscopy is based on the Bohr-Einstein frequency relationship:

$$\Delta E=E_2-E_1=h\,f \qquad (2.4.1)$$

This relationship links the discrete atomic or molecular energy states E_1 with the frequency f of the electromagnetic radiation. The proportionality constant h is Planck's constant (6.626×10^{-34} J s). In spectroscopy, it is appropriate to use the wavelength v instead of frequency f. Equation (2.4.1) then takes the form:

$$\Delta E=E2-E1=h\,c\,v$$

where,

$$f= c/\lambda =c\,v \qquad (2.4.2)$$

The Bouguer-Lambert-Beer law forms the mathematical-physical basis of light-absorption measurements on gases and solutions in the UV-VIS and IR-region[48], [49].

Spectroscopic methods of chemical analysis, which include UV-Vis spectrophotometry, are widely used to solve various chemical problems related to structure, kinetics, identification and quantitative analysis of various compounds.

In the visible spectroscopy study, a beam of radiation is directed to the test sample. The measurement of the radiation emitted by the sample is followed. Specifically, when

measuring in quartz cuvettes (UV-VIS region) or cuvettes made of special optical glass (VIS region), part of the light is lost through reflection at the cuvette surfaces. In order to eliminate this source of error, a reference measurement is made in a cuvette with the same path length but not containing the substance to be measured. Since most UV-VIS spectroscopy is carried out with solutions, the standard cuvette contains the pure solvent, which ideally should not absorb in the spectral region under consideration.

In order to determine the absorbed radiation, we compare the intensity of the outflow beam from the cuvette to the sample containing the chemical species that absorb with the intensity of the beam coming out of the reference cuvette. The reference cuvette contains a blank sample that does not contain the test substance (or substance of interest). The intensity of the radiation emanating from the blank sample is considered to be the corrected intensity of the radiation incident to the sample. This intensity is practically equal to the actual intensity of the incident because the losses in the blank sample (due to scattering, reflection or absorption) are very small.

Energy absorption requires a physical interaction between a photon and a particle of the chemical species that absorbs in the sample. The study of this absorption has led to the following equation:

$$dI_a = -kI_a cddo \qquad (2.4.3)$$

where,

k is a ratio constant, *c* is the concentration of the light-absorbing substance and *d* is the pathlength of the sample in cm. I_o is the intensity of the monochromatic light entering the sample and I_δ is the intensity of this light emerging from the sample. The negative sign is introduced because the intensity, I, decreases as the absorption layer becomes thicker. After completion the above equation (2.4.3) gives:

$$\log\frac{I_\delta}{I_0} = \frac{-k}{2{,}303}dc \qquad (2.4.4)$$

The fraction of the incident intensity exiting the sample defines the permeability, the latter

equation is transformed as:

$$\log T_0 = -\varepsilon_0 dc \qquad (2.4.5)$$

And also:

$$\frac{k}{2{,}303} = \varepsilon_0 \qquad (2.4.6)$$

$$A_0 = -\log T_0 \qquad (2.4.7)$$

where,

ε_o is the molar decadic extinction coefficient. The molar decadic extinction coefficient is a quantity characteristic of the substance which also depends on wavenumber v (cm^{-1}) or wavelength λ (nm). The functional correlation between ε_o and wavenumber v is called the "absorption spectrum" of a compound. Since the extinction coefficient can vary by several orders of magnitude within the absorption spectrum of a single inorganic or organic compound, the logarithmic value log ε_o = f(v) can be used to plot an absorption spectrum. The Bouguer-Lambert-Beer law is a limiting law for dilute solutions, i.e. the assertion that the extinction coefficient is independent of the concentration of a substance at the given wavenumber (or wavelength) applies only to dilute solutions.

The equation that arises is:

$$A_0 = -\varepsilon_0 dc \qquad (2.4.8)$$

The (2.4.8) equation is known as the Beer-Lambert law. The Beer-Lambert law assumes that the radiation is monochromatic, the chemical species they absorb display no interactions, the cross section of the sample is uniform, no fluorescence phenomena are observed and the concentrations in the active ingredients of the solutions from which the samples originate are small.

It is very common to express the concentration of solutions in terms of percentages. The percentage concentration is calculated as the fraction of the weight or volume of the

solute related to the total weight or volume of the solution. When the percentage concentration is calculated by weight, ε_0 is replaced by α_0 and the Beer-Lambert law is modified in the form bellow:

$$A_0 = -adc_m \qquad (2.4.9)$$

where:

c_m: is the concentration of the substance calculated in g L^{-1}

d: is the pathlength of the sample (practically corresponds, as mentioned above, to the thickness of the cuvette usually 1 cm)

α: absorbance

The graph of the absorption relative to the concentration is linear.

2.5 Electron Microscopy

2.5.1 Field Emission Scanning Electron Microscopy (FESEM)

Field emission scanning electron microscopy (FESEM) provides topographical and elemental information at magnifications of 10x to 300,000x, with virtually unlimited depth of field. Compared with the conventional scanning electron microscopy (SEM), field emission SEM (FESEM) produces clearer, less electrostatically distorted images with spatial resolution down to 1 1/2 nanometers – three to six times better. FESEM offers i) the ability to examine smaller-area contamination spots at electron accelerating voltages compatible with energy dispersive spectroscopy (EDS), ii) high-quality, low-voltage images with negligible electrical charging of samples (accelerating voltages ranging from 0.5 to 30 kilovolts) and iii) essentially no need for placing conducting coatings on insulating materials.

A field emission scanning electron microscope (FESEM) scans a focused electron beam

over a surface to create an image. The electrons in the beam interact with the sample, producing various signals that can be used to obtain information about the surface topography and composition. The electrons pass along a cylindrical column by means of magnetic coils spaced apart along the column. The focused electron beam is deflected on the x and y axes and the three-dimensional image is a result of the different angle of incidence of the beam at each point in the sample.

ii)Sputtering:

The samples were sputter-coated with gold in order to become more conductive. After the attachment of the samples on a specimen stub using a double-sided adhesive tape, the samples were ready for the FESEM analysis.

2.5.2 Transmission electron microscopy (TEM)

The transmission electron microscope (TEM) is an essential tool in all fields of scientific research including semiconductor development, biology and materials science. TEM is a microscopy technique in which a beam of electrons is transmitted through a specimen to form an image. The transmission electron microscopy advanced the industry standards, since it provides high resolution images and shows analytical capabilities. Transmission electron microscopes are capable of imaging at a significantly higher resolution than light microscopes, owing to the smaller de Broglie wavelength of electrons.

Theoretically, the maximum resolution, *d*, that one can obtain with a light microscope has been limited by the wavelength of the photons that are being used to probe the sample, λ, and the numerical aperture of the system, *NA*[50].

$$d = \lambda/(2nsin\alpha) \approx \lambda/(2NA)$$

where n is the index of refraction of the medium in which the lens is working and α is the maximum half-angle of the cone of light that can enter the lens.

From the top down, the TEM consists of an emission source or cathode, which may be a tungsten filament or needle, or a lanthanum hexaboride (LaB_6) single crystal source [51].

An electron gun, which has high brightness and high emission stability, is very effective for high-sensitivity analysis of a micro area down to several nanometers, as well as for high-resolution imaging. When you observe materials susceptible to radiation damage by a highly accelerated electron beam, such as carbon nanotubes and polymer materials, you can easily select the optimum accelerating voltage according to materials. The gun is connected to a high voltage source (typically ~100–300 kV) and, given sufficient current, the gun will begin to emit electrons either by thermionic or field electron emission into the vacuum. In the case of a thermionic source, the electron source is typically mounted in a Wehnelt cylinder to provide preliminary focus of the emitted electrons into a beam while also stabilizing the current using a passive feedback circuit. A field emission source uses instead electrostatic electrodes called an extractor, a suppressor, and a gun lens, with different voltages on each, to control the electric field shape and intensity near the sharp tip. The combination of the cathode and these first electrostatic lens elements is often collectively called the "electron gun". After it leaves the gun, the beam is typically accelerated by a series of electrostatic plates until it reaches its final voltage and enters the next part of the microscope; the condenser lens system. These upper lenses of the TEM then further focus the electron beam to the desired size and location on the sample [52]. This established electron optical system usually includes a rotation- and distortion-free imaging system and an α selector function for the variation of the electron-beam illumination angles. The optical conditions of TEM, such as probe diameter and camera length, are optimized for observations using the scanning modes (STEM-BF/DF/HAADF, BEI,SEI) and analyses (EDS, EELS). These optimized conditions are immediately retrieved through a GUI.

Manipulation of the electron beam is performed using two physical effects. The interaction of electrons with a magnetic field will cause electrons to move according to the left-hand rule, thus allowing for electromagnets to manipulate the electron beam. The use of magnetic fields allows for the formation of a magnetic lens of variable focusing power, the lens shape originating due to the distribution of magnetic flux. Additionally, electrostatic fields can cause the electrons to be deflected through a constant angle.

2.6 Dynamic Light Scattering (DLS)

The Dynamic Light Scattering (DLS) method is the most common measuring technique in the nanometer range for particle size analysis. Dynamic light scattering (DLS) is based on the Brownian motion of dispersed particles. When particles are dispersed in a liquid they move randomly in all directions. The principle of Brownian motion is that particles are constantly colliding with solvent molecules. These collisions cause a certain amount of energy to be transferred, which induces particle movement. The energy transfer is more or less constant and therefore has a greater effect on smaller particles. As a result, smaller particles are moving at higher speeds than larger particles. If you know all other parameters which have an influence on particle movement, you can determine the hydrodynamic diameter by measuring the speed of the particles.

The relation between the speed of the particles and the particle size is given by the Stokes-Einstein equation (2.6.1). The speed of the particles is given by the translational diffusion coefficient *D*. Further, the equation includes the viscosity of the dispersant and the temperature because both parameters directly influence particle movement. A basic requirement for the Stokes-Einstein equation is that the movement of the particles needs to be solely based on Brownian motion. If there is sedimentation, there is no random movement, which would lead to inaccurate results. Therefore, the onset of sedimentation indicates the upper size limit for DLS measurements. In contrast, the lower size limit is defined by the signal-to-noise ratio. Small particles do not scatter much light, which leads to an insufficient measurement signal.

$$D=kBT6\pi\eta RH \qquad (2.6.1)$$

where,

D: Translational diffusion coefficient [m²/s] – "speed of the particles"
k_B:Boltzmann constant [m²kg/Ks²]
T: Temperature [K]

h:Viscosity[Pa.s]

R_H: Hydrodynamic radius [m]

The basic setup of a DLS instrument is shown in Figure 12. A single frequency laser is directed to the sample contained in a cuvette. If there are particles in the sample, the incident laser light gets scattered in all directions. The scattered light is detected at a certain angle over time and this signal is used to determine the diffusion coefficient and the particle size by the Stokes-Einstein equation.

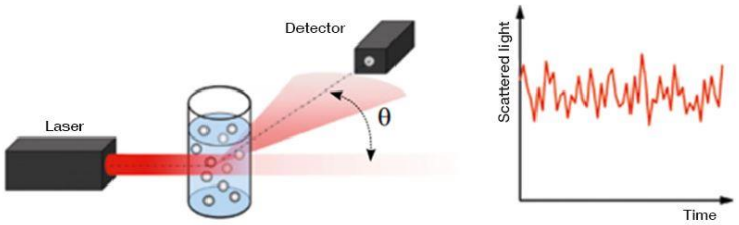

Fig. 8 Basic setup of a DLS measurement system. The sample is contained in a cuvette. The scattered light of the incident laser can be detected at different angles.

The incident laser light is usually attenuated by a gray filter which is placed between the laser and the cuvette. The filter settings are either automatically adjusted by the instrument or can be set manually by the user.

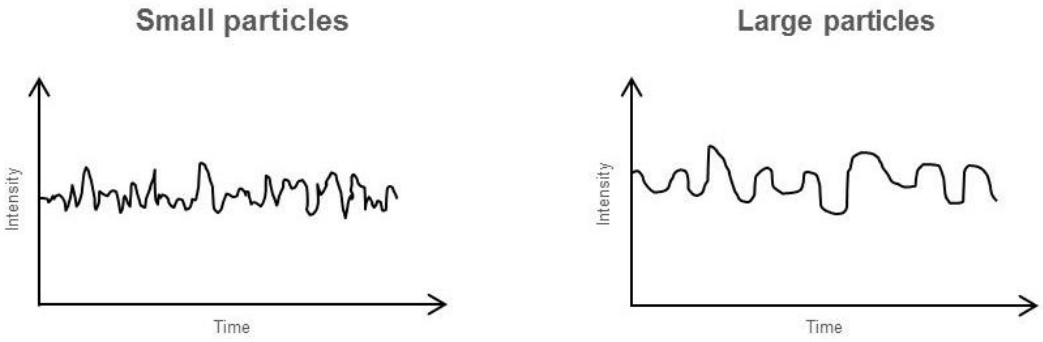

Fig. 9 Differences in the intensity trace and correlation function of large and small particles. Smaller particles show faster fluctuations of the scattered light and a faster decay of the correlation function.

When turbid samples are measured, the detector would not be able to process the number of photons. Therefore, the laser light is attenuated to receive a sufficient but processable signal at the detector [53].

The scattered light is detected over a certain time period in order to monitor the movement of the particles. The intensity of the scattered light is not constant but will fluctuate over time. Smaller particles, which are moving at higher speeds, show faster fluctuations than larger particles. On the other hand, larger particles result in higher amplitudes between the maximum and minimum scattering intensities, as shown in Figure 9.

The polydispersity index (PDI) is given in order to describe the broadness of the particle size distribution. The polydispersity index is also calculated by the cumulant method. A value below 10 % reflects a monodisperse sample and indicates that all of the measured particles have almost the same size. Generally, the polydispersity index is considered good when it does not exceed the value of 30%. However, the polydispersity index does not provide any information about the shape of the size distribution or the ratio between two particle fractions.

2.7 Zeta Potential

Over the last few decades zeta potential measurements have become an important characterization method for surface functionality or stability of dispersed particles. Zeta potential assessment focuses primarily on obtaining data about a material's surface charge. The material can range from colloidal nanoparticles up to macroscopic surfaces like membranes or silicon wafers [54].

The zeta potential (also known as electrokinetic potential) is established on the surface of any material when it comes in contact with a liquid medium. It is therefore an interfacial property and is usually provided in a unit of millivolt.

If a substance goes into contact with a liquid, the surface of the functional groups will react with the surrounding medium. This process results in a surface charge, which attracts the accumulation of oppositely charged ions. These counter ions arrange themselves spontaneously in a so-called electrochemical double layer. The zeta potential is defined as the sum of the initial surface charge and the accumulated layer. The zeta potential is present only when a material comes into contact with a liquid and it represents the effective net charge in this condition. Moreover, it can be measured on macroscopic surfaces (e.g. membranes, hair, polymers) as well as from particles dispersed in a liquid (e.g. colloids, nanoparticles, liposomes). The properties of the liquid medium play an important role in the formation of the zeta potential, which is highly dependent on the pH value or buffer concentration. Measuring the zeta potential provides information on surface functionality, the stability of dispersed particles as well as interaction of dissolved compounds with the solid surface.

The zeta potential of particles is a key indicator of the stability of a colloidal dispersion, like nanoparticles or liposomes, since it reflects the ability of particles to repulse each other electrostatically. Empirically, it is considered that absolute zeta potential values higher than ± 30 mV are indicative of very stable dispersions. Only the magnitude of the zeta potential indicates the stability of the sample, whereas the sign of the zeta potential shows whether positive or negative charges are dominant at the surface. Below ± 30 mV processes like aggregation, sedimentation, and/or flocculation are more likely.

Charge formation occurs due to i) reactions of functional groups or ii) adsorption of ions from the solution. Charge formation by reaction of functional groups is based on acidic and basic surface groups. Acidic groups such as carboxylic or sulfonic acid dissociate when in contact with water, i.e. the H+ ion is released into the surrounding water and the surface assumes a negative charge [55]. Basic groups such as amine groups become protonated when in contact with water, i.e. the surface assumes a positive charge. The equilibrium of dissociation and protonation is strongly dependent on the pH value of the liquid medium and therefore has a strong influence on the formed surface charge of the material and further on the zeta potential [54],[55].

2.8 Photoluminescence Spectroscopy

Photoluminescence spectroscopy is a contactless, nondestructive method of probing the electronic structure of materials. Light is directed onto a sample, where it is absorbed and imparts excess energy into the material in a process called photo-excitation. One way this excess energy can be dissipated by the sample is through the emission of light, or luminescence. In the case of photo-excitation, this luminescence is called photoluminescence [56]. Photo-excitation causes electrons within a material to move into permissible excited states. When these electrons return to their equilibrium states, the excess energy is released and may include the emission of light (a radiative process) or may not (a nonradiative process). The energy of the emitted light (photoluminescence) relates to the difference in energy levels between the two electron states involved in the transition between the excited state and the equilibrium state. The quantity of the emitted light is related to the relative contribution of the radiative process.

Photoluminescence is divided into two categories: fluorescence and phosphorescence. A pair of electrons occupying the same electronic ground state have opposite spins and are said to be in a singlet spin state. When an analyte absorbs an ultraviolet or visible photon, one of its valence electrons moves from the ground state to an excited state with a conservation of the electron's spin. Emission of a photon from the singlet excited state to the singlet ground state—or between any two energy levels with the same spin—is called fluorescence [57]. When the chemical substrate undergoes internal energy transitions before relaxing to its ground state by emitting photons, some of the absorbed energy is dissipated so that the emitted light photons are of lower energy than those absorbed. One of such most familiar phenomenon is fluorescence, which has a short lifetime (10^{-8} to 10^{-5} s). Fluorescence, therefore, decays rapidly once the source of excitation is removed. Due to the fact that molecules return to their ground state by the fastest mechanism, fluorescence is observed only if it is a more efficient means of relaxation than a combination of internal conversions and vibrational relaxations. A quantitative expression of fluorescence efficiency is the fluorescent quantum yield, Φ_f, which is the fraction of excited state molecules returning to the ground state by fluorescence. Fluorescent

quantum yields range from 1, when every molecule in an excited state undergoes fluorescence, to 0 when fluorescence does not occur. The intensity of fluorescence, I_f, is proportional to the amount of radiation absorbed by the sample, $P_0 - P_T$, and the fluorescent quantum yield emission. Fluorescence is generally observed when the molecule's lowest energy absorption is a $\pi \rightarrow \pi^*$ transition, although some $n \rightarrow \pi^*$ transitions show weak fluorescence. Most unsubstituted, non heterocyclic aromatic compounds have favorable fluorescence quantum yields, although substitutions on the aromatic ring can significantly effect Φ_f. For example, the presence of an electron-withdrawing group, such as $-NO_2$, decreases Φ_f, while adding an electron-donating group, such as –OH, increases Φ_f. Fluorescence also increases for aromatic ring systems and for aromatic molecules with rigid planar structures [58].

In some cases an electron in a singlet excited state is transformed to a triplet excited state in which its spin is no longer paired with the ground state. Emission between a triplet excited state and a singlet ground state—or between any two energy levels that differ in their respective spin states–is called phosphorescence. Because the average lifetime for phosphorescence ranges from 10^{-4}–10^4 s, phosphorescence may continue for some time after removing the excitation source [59].

2.9 Cell Culture Maintenance

In this project we examined three different cell populations; one of them was mesenchymal and the other two were cancer cell lines. Concerning the mesenchymal cells we used WJ-MSC cells. The Wharton's Jelly mesenchymal cells, is an anchorage dependent cell line and is cultured while attached to a solid or semi-solid substrate. Wharton's Jelly cells are derived from the inner jelly substance in the umbilical cord and are isolated from a single donor. These cells have characteristics of MSCs and are widely investigated for their use in therapeutic applications [63]. On the other hand, for the cancer cell lines we used HCT116 and WM164. HCT116 is a human colon cancer cell line with a mutation in

codon 13 of the ras proto-oncogene. The HCT116 cells are adhesive and have a characteristic epithelial morphology [60],[61]. WM164 is a metastatic human melanoma cell line established from a metastatic site. This cell line features the specific V600E (Val600Glu) mutation at codon 600 in the BRAF gene. This mutation causes constitutively active kinase activity and activation of MEK and ERK signaling pathway [62].

WJ-MSC cells were cultured in DMEM/F12 (with 3.5 g/L glucose, ultraglutamine I, and Na pyruvate; Lonza) supplemented with 10% batch-tested fetal bovine serum (FBS), 15 mM HEPES, 1x nonessential amino acids, and 1% penicillin/streptomycin (all from Invitrogen). Cancer cells were cultured in DMEM, 10% FBS, 1% Penicillin/ STREPTOMYCIN and 1% mem non-essential amino acids.

All cells are cultured in an incubator that supplies 5% CO_2 in air and regulates the physicochemical environment at 37°C in a humidified atmosphere. The size of the flasks vary, as well as the amount of the culture medium that was added, according to the number of cells that were seeded. Small flasks of 25 cm^2 were seeded with 1-2 x 10^5 cells in 5 mL culture medium and large flasks of 75 cm^2 were seeded with 3-4 x 10^5 cells in 10 mL culture medium. Confluent cells are harvested from the culture flasks using trypsin/EDTA and counted on a haemocytometer. Trypsin is a proteolytic enzyme that is formed in the intestine by trypsinogen. Its effect lies in catalyzing the hydrolysis of peptide bonds in partially cleaved proteins. In particular, it cuts the amino terminus in lysines and arginines if they are not followed by proline. The inhibition of trypsin action is accomplished by injecting culture medium equal or twice as high as the trypsin that was plated [63].

2.10 Cytotoxicity Assay

The proliferation of WJ-MSC, HCT116 and WM164 cells was assessed using the MTS assay, the role of which is the staining of living cells. The MTS assay protocol is based on the reduction of the MTS tetrazolium compound by viable cells to generate a colored formazan dye that is soluble in cell culture media. This conversion is thought to be carried out by

NAD(P)H-dependent dehydrogenase enzymes in metabolically active cells. The formazan dye is quantified by measuring the absorbance at 490-500 nm. The dye used to make the solution was diluted at 1:5 ratio in culture media. Before the addition of the MTS solution, the supernatant that contained the NPs was removed and the cells were washed with PBS (Phosphate Buffered Saline). Afterwards, the MTS solution was added in the polystyrene plates, the plates were placed back in the incubator for 1, 2 and 3 hours for colour development. Colour development was detected spectrophotometrically at 490/500 nm and according the absorption, a living cell evaluation was provided.

Every experiment was performed in triplicates and it was an end-point experiment after the measurement of the absorption.

Protocol (step by step):

i. Culture cells (5 – 100 x 103/well) in a 96-well microtiter plate in a final volume of 200 µL/well

ii. Incubate cells for 48 hours.

iii. After 48 hours add 20 µL/well MTS Reagent into each well and incubate for 1, 2 and 3 hours at 37°C in standard culture conditions.

iv. The measurement was then made, after placing the 96-well plate in the spectrophotometer and calculated the absorption at 490/500 nm.

Before assessing the cytotoxicity levels of the polymer NPs, we performed tests on WJ MSC HCT116 and WM164 cells seeded in TCPS plates. Standard curves were prepared for cells seeded in 96-well plates using abs (490/500) as the mode of detection for the MTS reagent color change.

3. Results and Discussion

3.1 Synthesis of Polymers

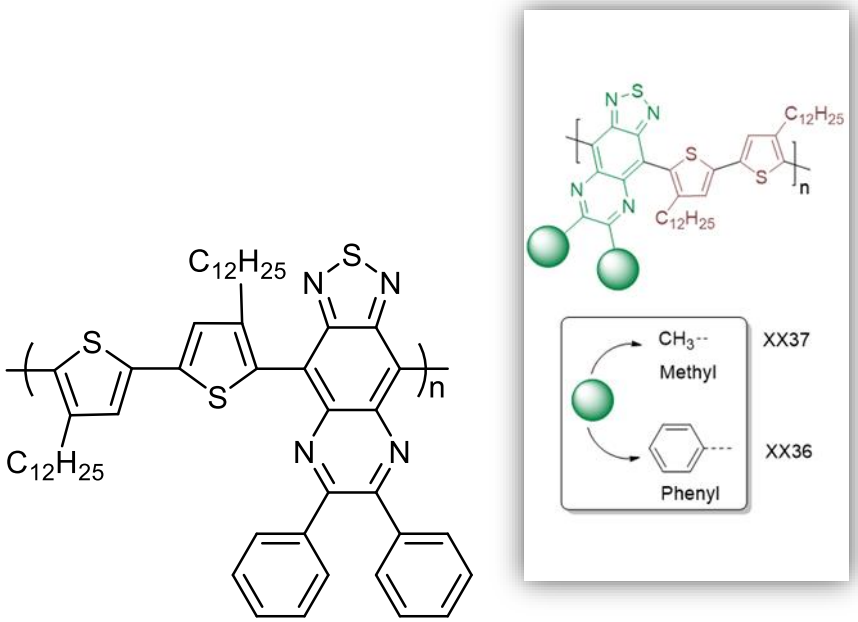

Fig. 10: A schematic representation of BTTDQ-Ph CPs.

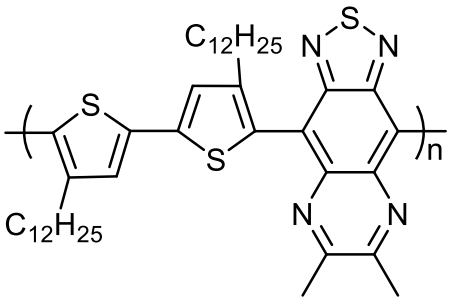

Fig. 11: A schematic representation of BTTDQ-Me CPs.

As it was thoroughly described in section *(2.1)*, different conjugated polymers were synthesized consisting of thiadiazoloquinoxaline biphenyl substituted-bithiophene and thiadiazoloquinoxaline bimethyl substituted-bithiophene, BTTDQ-Ph and BTTDQ-Me, respectively. In Fig. 15 a real depiction of the final products i.e BTTDQ-Ph and BTTDQ-Me

CPs is given. This characteristic chemical structure is also confirmed in the next section (3.2) of the ^{1}H-NMR assay.

Fig. 12: Solutions of BTTDQ-Ph and BTTDQ-Me CPs.

When the BTTDQ-Ph and BTTDQ-Me conjugated polymers are dissolved in THF, colour-based solutions are obtained (*Fig.12).* On the left, the BTTDQ-Me CP with a characteristic blue colour and on the right the blue-green solution of BTTDQ-Ph are depicted. The solubility of the BTTDQ-Me CP in the THF was clearly poorer than the corresponding one of the BTTDQ-Ph CP, due to the stronger aggregation that takes place in the methyl substituted CP. Thus, the methyl-substituted required more hours to dissolve.

3.2 ^{1}H-NMR

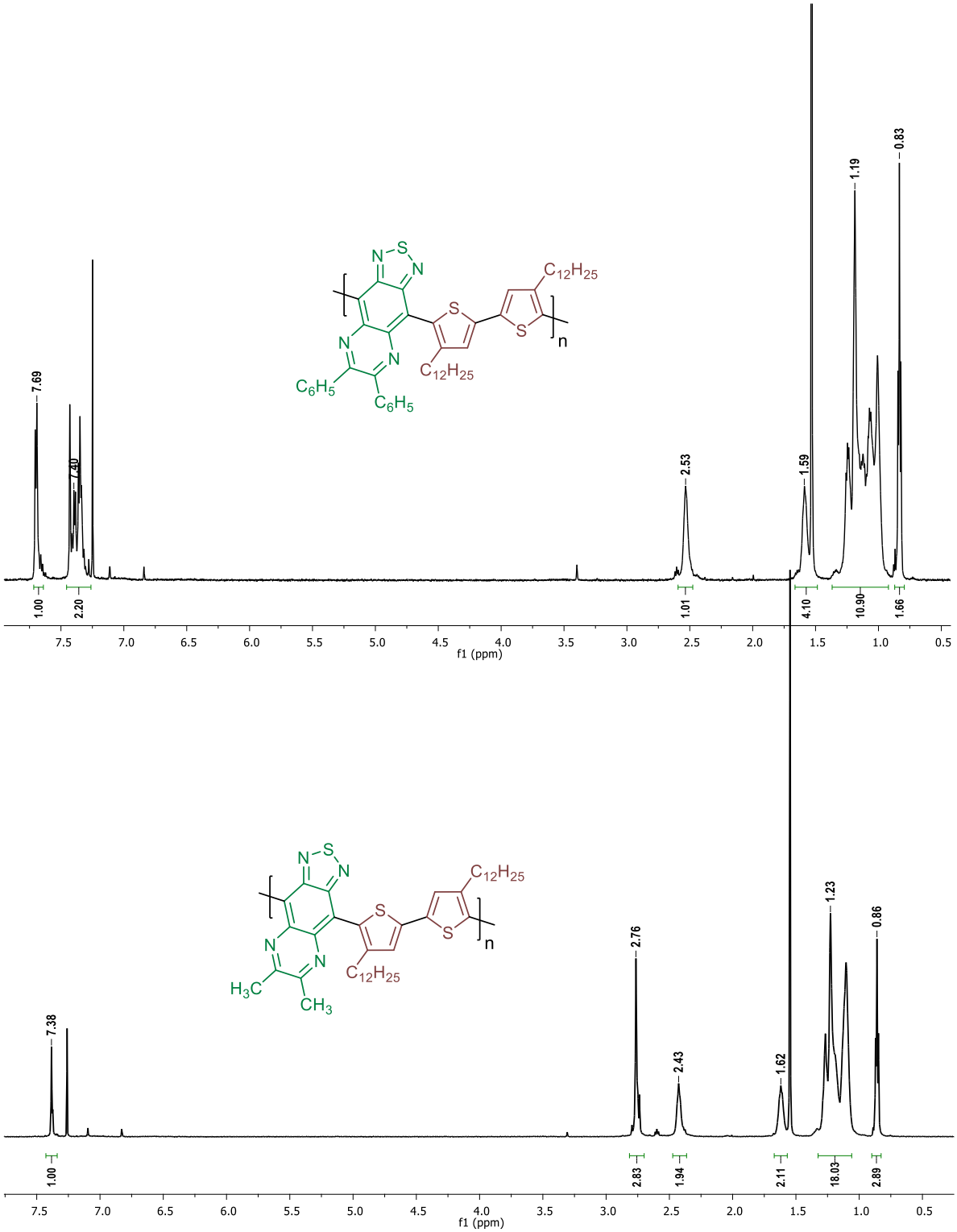

Fig. 13: ^{1}H-NMR spectra of BTTDQ phenyl (a) and methyl substituted (b).

In figure 13 a and b, the ^{1}H-NMR spectra of BTTDQ-Ph and BTTDQ-Me are given. In both spectra the upfield region between 0.83 to 1.59 ppm and 0.86 to 1.62 ppm, for the BTTDQ-Ph and BTTDQ-Me, respectively, refers to the remote protons boned to the aliphatic carbon atoms. The hydrogens of thiophene's aliphatic adjacent carbons are displayed at 2.43 ppm and 2.53 ppm and the peak at 2.76 ppm corresponds to 3H of methyl substituted BTTDQ. The most protected proton of thiophene ring displayed at 7.38 and 7.45 ppm while the peaks at 7.35ppm, 7.42ppm, and 7.71ppm corresponds to phenyl ring protons of BTTDQ-Ph. Comparing the spectra, there is a significant chemical shift from 2.83 ppm to 7.40 ppm of the substituted benzothiazole quinoxaline. This chemical shift is attributed to the resonance phenomenon and the electron cloud, that shields the benzyl protons.

3.3 TEM and FESEM.

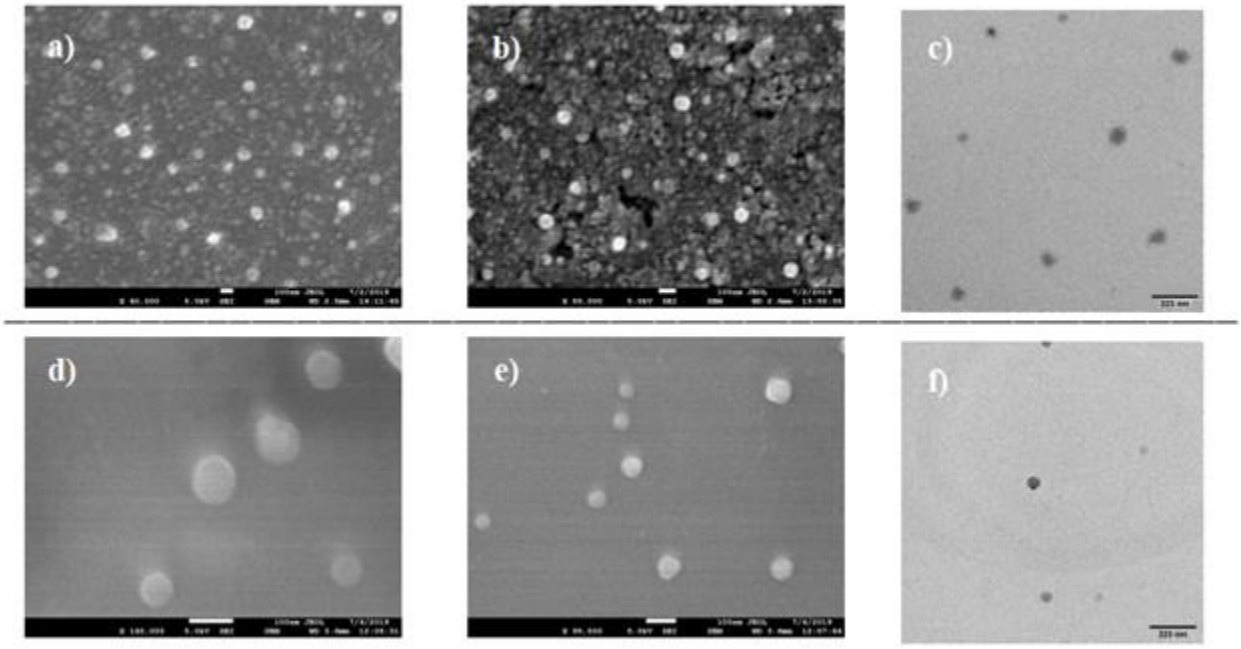

Fig. 14:FESEM (a,b) and TEM (c) images of BTTDQ-Ph and FESEM (d,e) and TEM (f) images of BTTDQ-Me NPs.

FESEM and TEM characterization revealed that the BTTDQ-Ph and BTTDQ-Me self-aggregate in water resulting in CPNs with a well-defined smooth spherical shape and an average diameter of 100 nm. The fact that the hydrophobic conjugated polymers successfully generate uniform nanoparticles without the addition of an amphiphilic molecule is considered as a great advantage, regarding their easy manufacturing and reproducibility [64]-[66]. Moreover, the spherical shape of water-soluble conjugated polymers was also witnessed in previous reports, confirming our results. The diameter of WSCPs that is mentioned in other reports ranges from 40 to 500 nm, based on the production technique and the monomers were used [67],[68]. The mean particle size observed from FESEM and TEM images is lower than that obtained by DLS measurements, which is mainly caused by the shrinkage of the polymeric NPs during the sample preparation in vacuum. A similar phenomenon has also been observed for other polymeric NPs [69],[70].

3.4 UV-VIS Spectroscopy

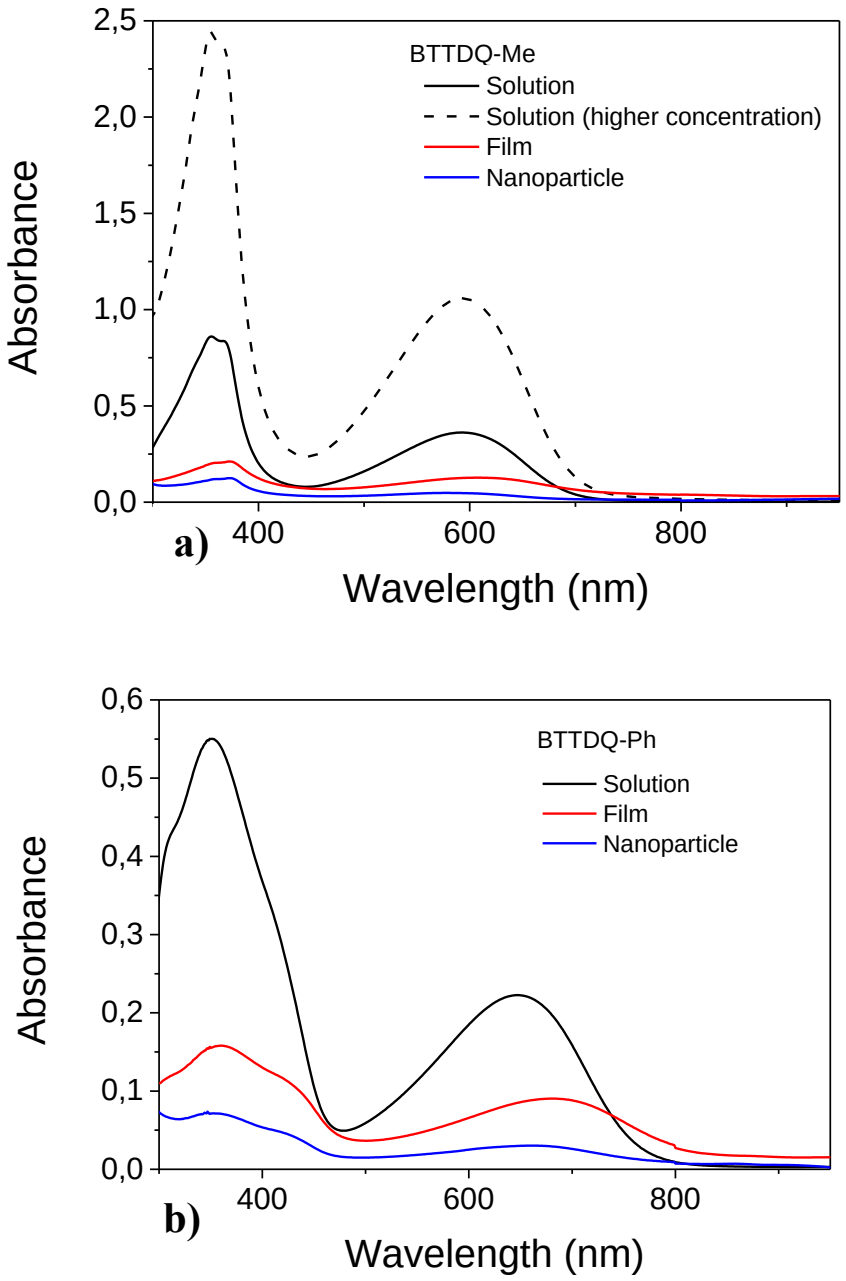

Fig. 15: UV-Vis absorption spectra of the low-bandgap BTTDQ-Ph (a) and BTTDQ-Me (b).NPs suspensions in solution, film and water.

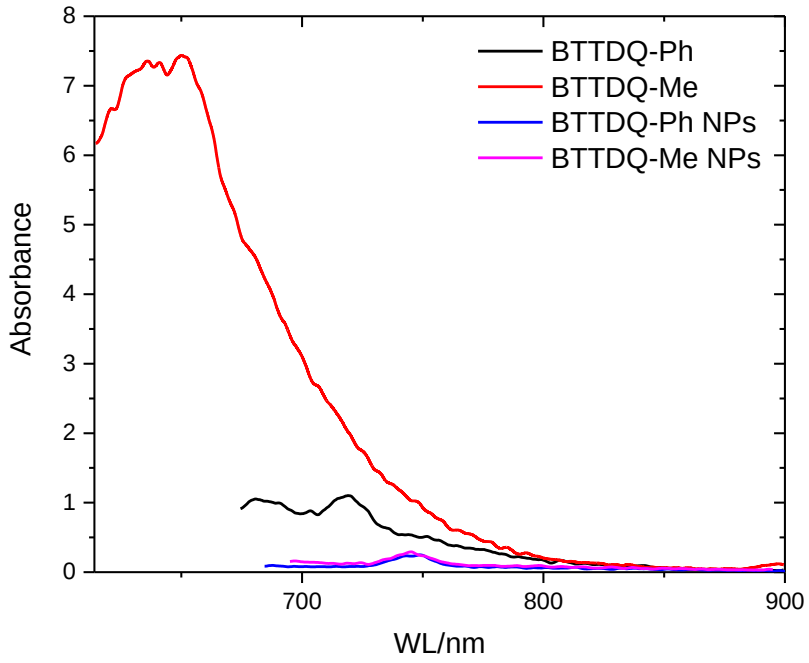

Fig. 16: Fluorescence spectra of the low-bandgap BTTDQ-Ph and BTTDQ-Me NPs suspensions in solution and water.

Figure 15(a,b) and Figure 16 show the UV-Vis absorption and fluorescence spectra of the low-bandgap BTTDQ-Ph and BTTDQ-Me NPs suspensions in water. The wavelength at which the polymer solution and NPs exhibit maximum UV-Vis absorbance and fluorescence intensity are shown in Table 2. The BTTDQ-Ph and BTTDQ-Me nanoparticles have low absorption in the yellow to red regions with λ_{max} at 660 and 580 nm, respectively. BTTDQ-Ph and BTTDQ-Me show significant light absorption in the UV-Vis region as shown in Figure 15 (a,b). Moreover, the absorption spectrum of each low-bandgap NPs exhibits a broadened and red-shifted absorption spectrum relative to that of the corresponding isolated low-bandgap conjugated polymer chains in THF solvent. The absorption peak at 660 and 580 nm, in BTTDQ-Ph and BTTDQ-Me, respectively arises from π–π* transition of the conjugated back-bone, while the broad absorption band from 600 to 800 nm results from charge transfer between bithiophene and thiadiazoloquinoxaline units. Moreover, the red-shifted emission wavelength possibly originates from the strong side chain static effect [71].

The fluorescence wavelengths of the CPNs in aqueous suspensions and the CPs in THF solution were measured using a photoluminesence spectometer. The emission maxima

for BTTDQ-Ph and BTTDQ-Me NPs are at 516 and 636 nm, respectively. The emission tail in the PL spectrum after 700 nm suggests that these NPs hold potential for in vivo FR/NIR imaging. The photoluminescence (PL) spectra of the BTTDQ-Ph solution display a high-energy peak at 720 nm that can be attributed to the polymers' backbone. The PL spectra of BTTDQ-Me exhibit a lower peak at 645 nm, which was expected and can be assigned to the methyl substitution. The photoluminescence (PL) spectra of the BTTDQ-Ph and BTTDQ-Me NPs though, mark a peak at the emission spectra at the 745 nm, slightly higher than the emission peaks of both BTTDQ-Ph and BTTDQ-Me solutions [72]-[74].

Table 2: Photophysical properties of CPNs.

Low-Bandgap Conjugated NPs	**BTTDQ-Ph**	**BTTDQ-Me**
Absorption / Fluorescence **λ_{max}^{NPs} (nm)**	660 / 745	580 / 745
Absorption / Fluorescence **λ_{max}^{sol} (nm)**	650 / 720	595 / 645

The strong emission (Table 2) was expected given the frequent use of benzothiadiazole in fluorescent materials and conjugated polymers [74]-[76]. The electronic character of the substituents in quinoxaline molecule strongly affects the absorption spectra producing a significant bathochromic shift to an extent which depends on their electron-donating ability. Higher the electron-donating ability of the donor groups present in the quinoxaline moiety, higher is the λ_{max} value [77].

3.5 DLS and Zeta Potential

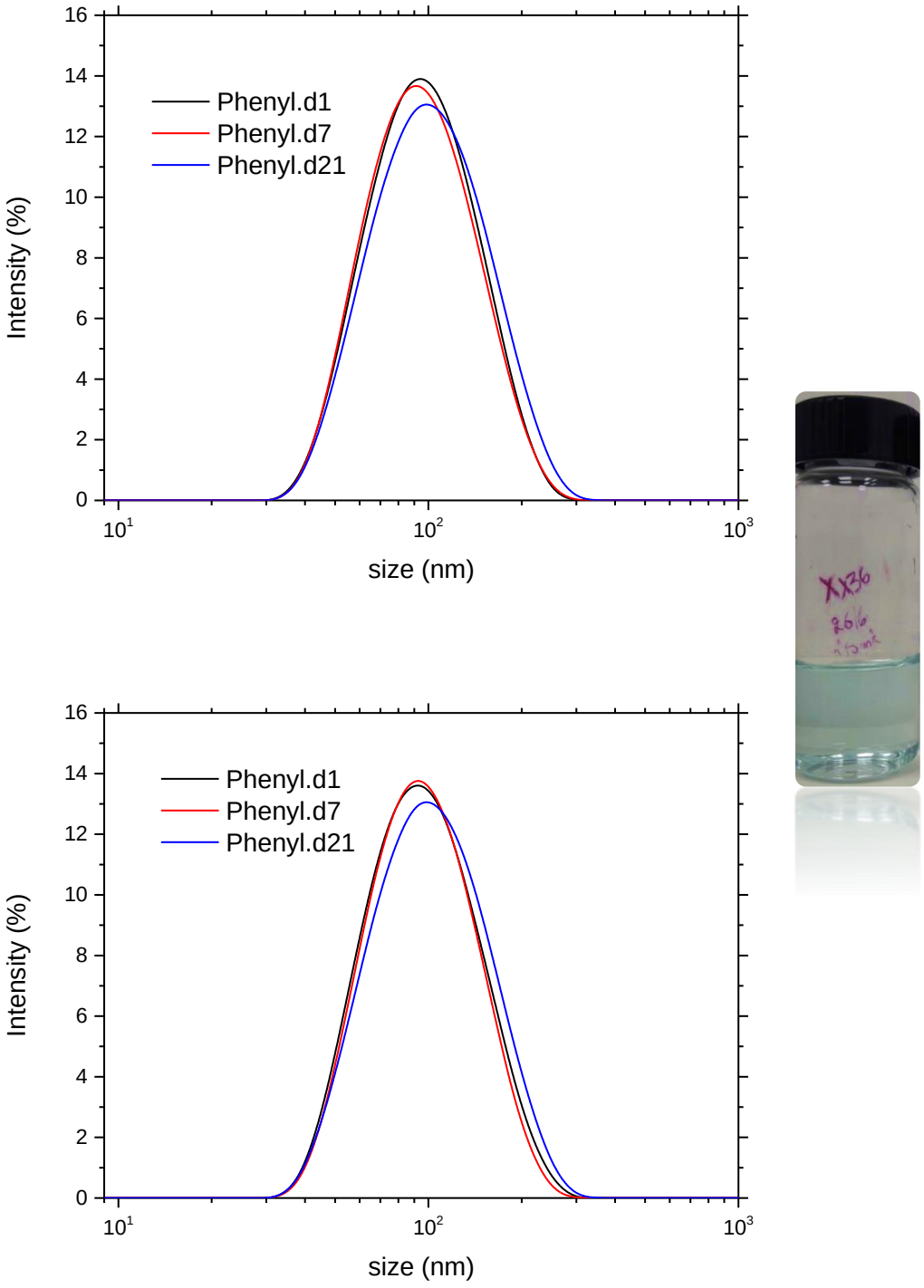

Fig. 17: Particle size distribution of BTTDQ-Ph NPs after 1, 7 and 21 days at 25 °C (a) and 37 °C (b).

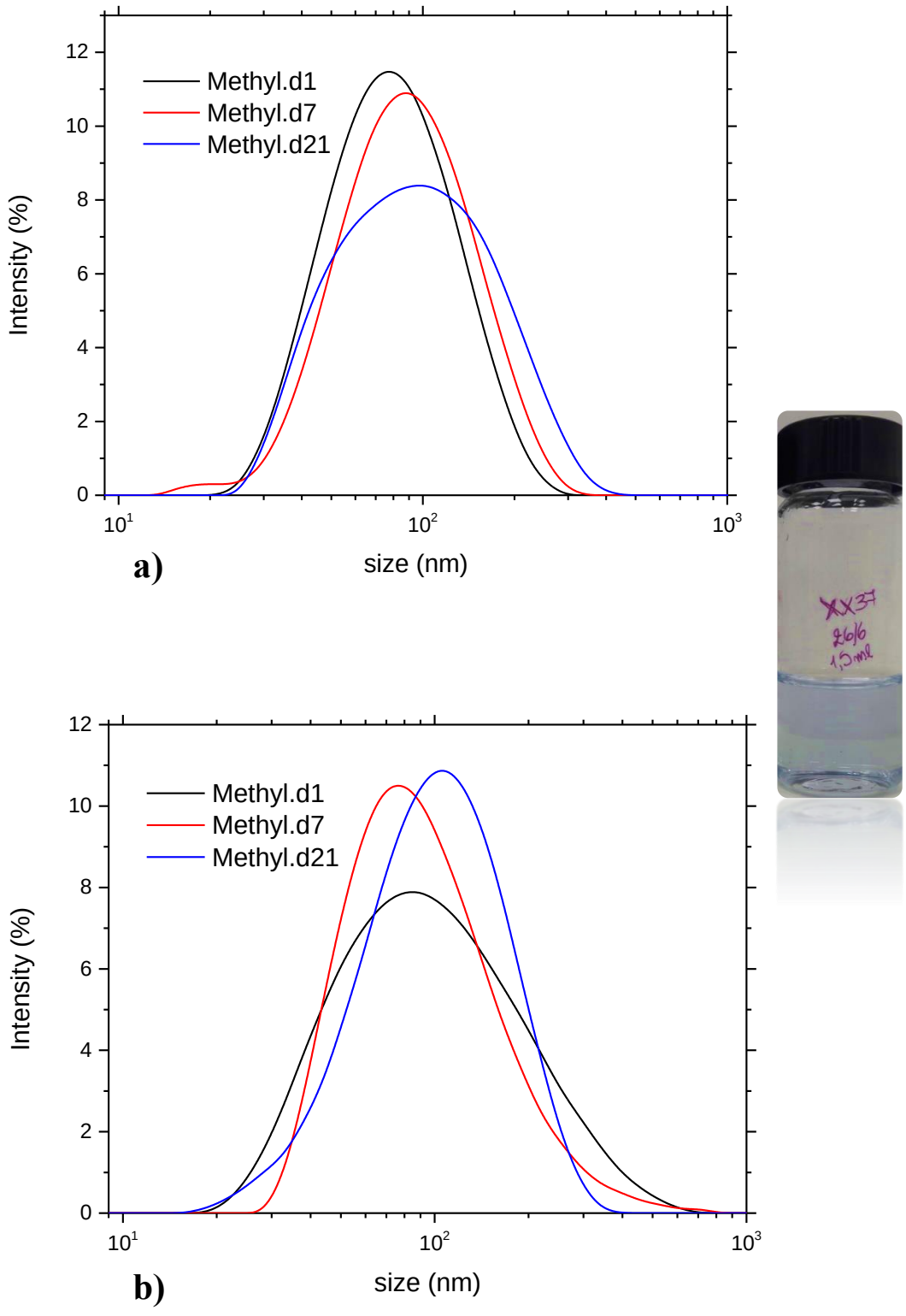

Fig. 18: Particle size distribution of BTTDQ-Me NPs after 1, 7 and 21 days at 25 °C (a) and 37 °C (b)

The low-bandgap CP nanoparticles display excellent colloidal stability in water, showing no sign of particle aggregation even after three weeks. The production of nanoparticles using the nanoprecipitation method is a surfactant-free approach and the colloidal stability arise from inherent surface characteristics of the conjugated polymer NPs. The resistance of low-bandgap CP NPs to undergo aggregation in water is attributable to a substantial and negative zeta potential, as shown in Fig. 19 and Fig. 20, ranging from –13 to –23 mV. It is well known that colloidal suspensions systems with zeta potential value of –25 mV or lower maintain a long-term colloidal stability [78],[79].

Generally, stable polymer nanoparticles in water obtain a micellar structure that consists of a hydrophobic core and a hydrophilic shell. However, the conjugated polymers used in this study would exhibit strictly hydrophobic characteristics. Therefore, we assume that chemical modification of the CP during the nanoparticles formation leads to hydrophilic defects and consequently in the desirable negative zeta potential [84]. The average size of the NPs was measured in two different temperatures (25 ^{o}C and 37^{o}C). 25 ^{o}C (temp.1) is attributed to the product maintenance temperature, whereas 37 ^{o}C (temp.2) to the normal temperature for the in vitro and for the in vivo experiments. The size of the BTTDQ-Ph NPs was 87.96±0.22 and 88.13±0.30 for 25 ^{o}C and 37^{o}C, respectively. In addition, BTTDQ-Me NPs have a size distribution of 73.58±0.64 and 73.27±0.25 for 25 ^{o}C and 37^{o}C, respectively. The width of the “curve bell” of the Gaussian distribution that the CPNs possess, is narrow and their polydispersity is below 0.3. The narrow polydispersity indicates a uniform polymer, also known as monodispersed. Moreover, according to previous studies the dimensions and the shape of the NPs are critical factors in order to the NPs escape from the endothelium. NPs >200 nm are cleared in the liver and spleen, while <10 nm are cleared from the kidneys. The optimal size for the NPs is considered to be between 10nm and 200 nm. In addition, they have to be close to 100 nm in order to escape the endothelium and reach the cancer tissue [80],[81].

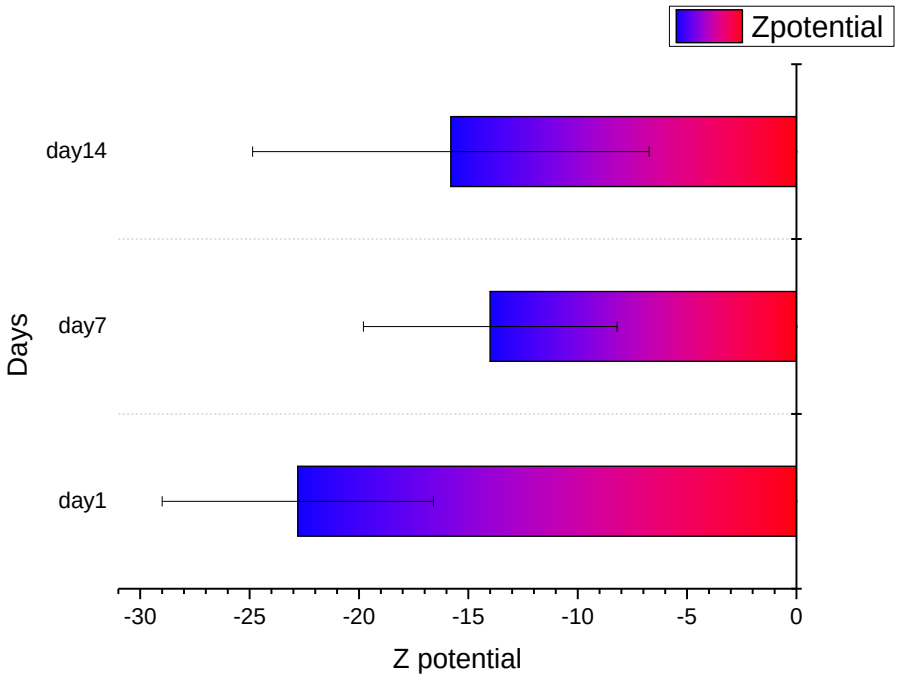

Fig. 19: Zeta potential measurements of BTTDQ-Ph NPs after 1, 7 and 14 days after their production.

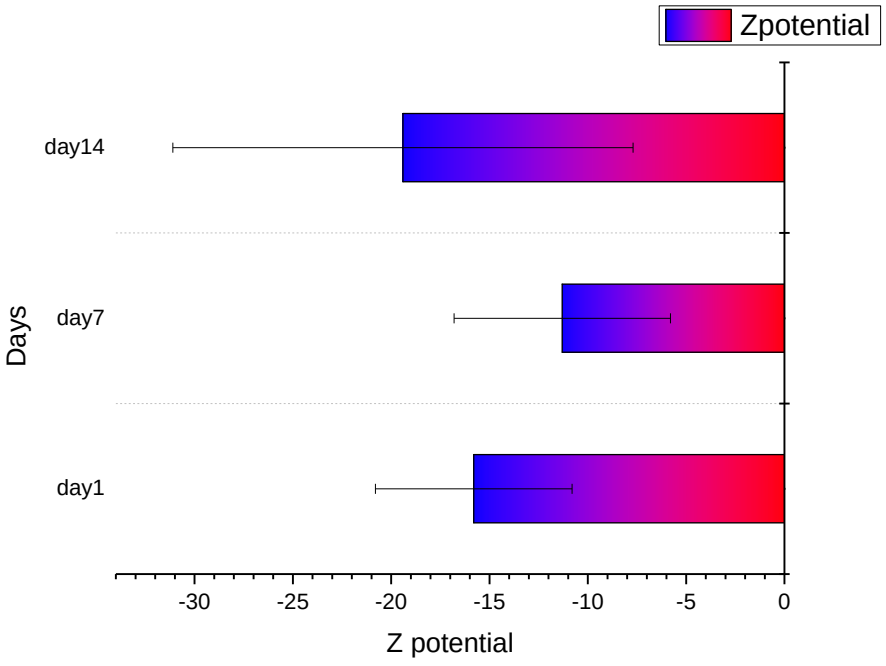

Fig. 20: Zeta potential measurements of BTTDQ-Me NPs after 1, 7 and 14 days after their production.

3.6 Cytotoxicity assay

The viability of cells on the polymeric NPs was quantitatively determined by the colorimetric MTS assay for 48 hours of culture. Absorbance of the bioreduced soluble formazan product was measured at 490 nm using a spectrophotometer. Results were quantified by subtracting the blank value from each value then normalizing against the control values [82]. The MTS assay was performed as a function of the NPs concentrations and the percentage of cell viability was determined. The ideal fluorescent cell trackers will minimally derange the functions of stem cells that are generally sensitive and fragile to exterior stimuli. To address this issue, the viability of MSCs treated with BTTDQ-Ph and BTTDQ-Me NPs was investigated by using NPs-free MSCs as control [83]. The in vitro proliferation of WJ-MSCs was assessed after labeling with different concentrations of BTTDQ-Ph and BTTDQ-Me NPs.

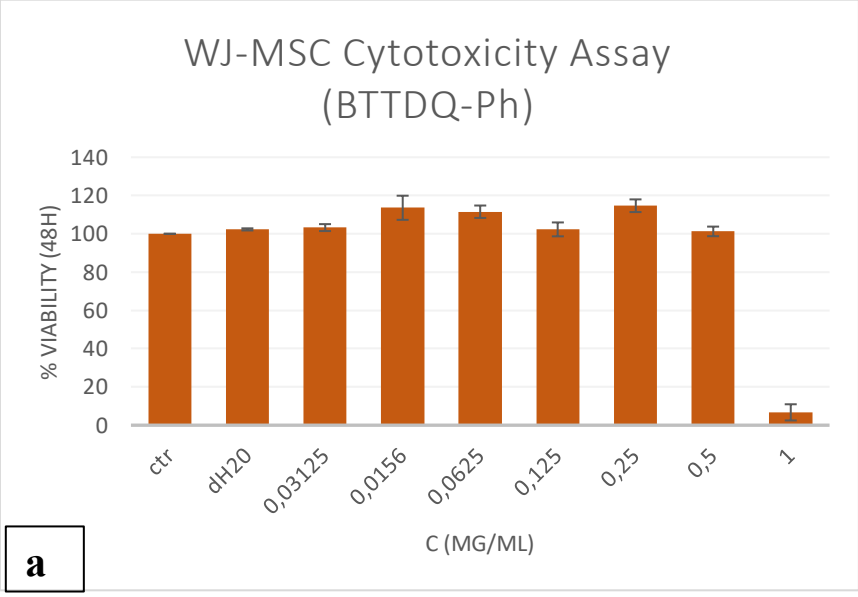

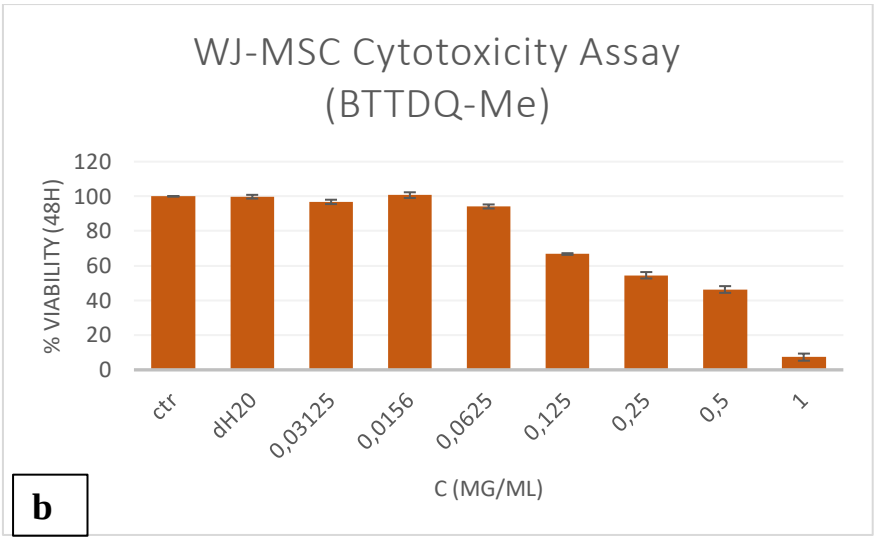

Fig. 21: Viability assay of WJ-MSC on BTTDQ-Ph (a) and BTTDQ-Me NPs (b).

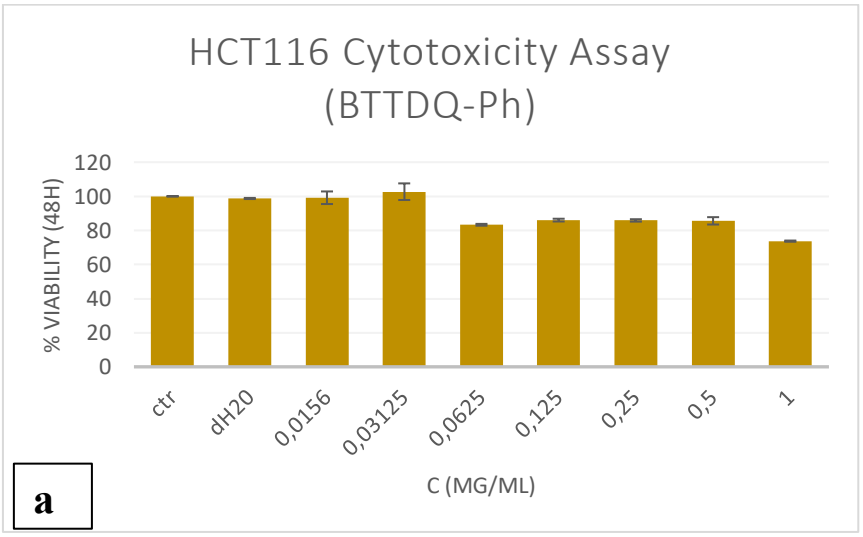

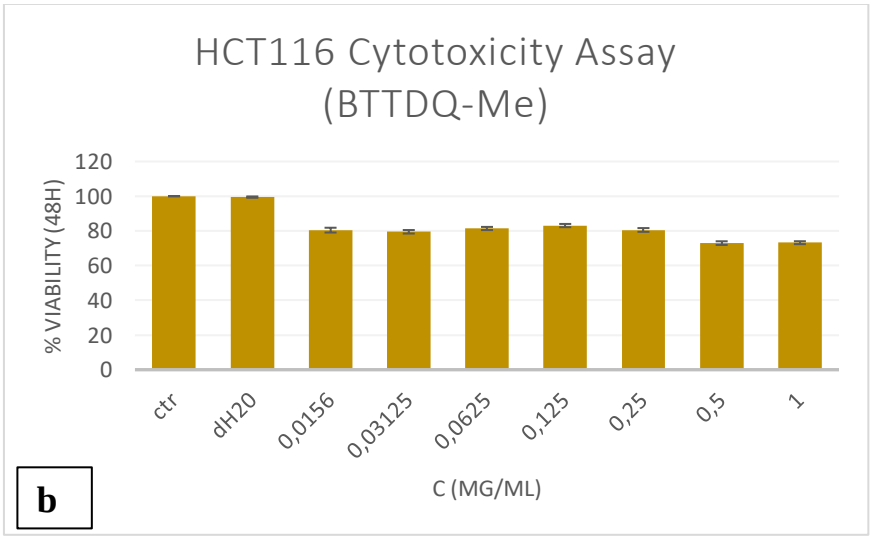

Fig. 22: Viability assay of HCT116 on BTTDQ-Ph (a) and BTTDQ-Me NPs (b).

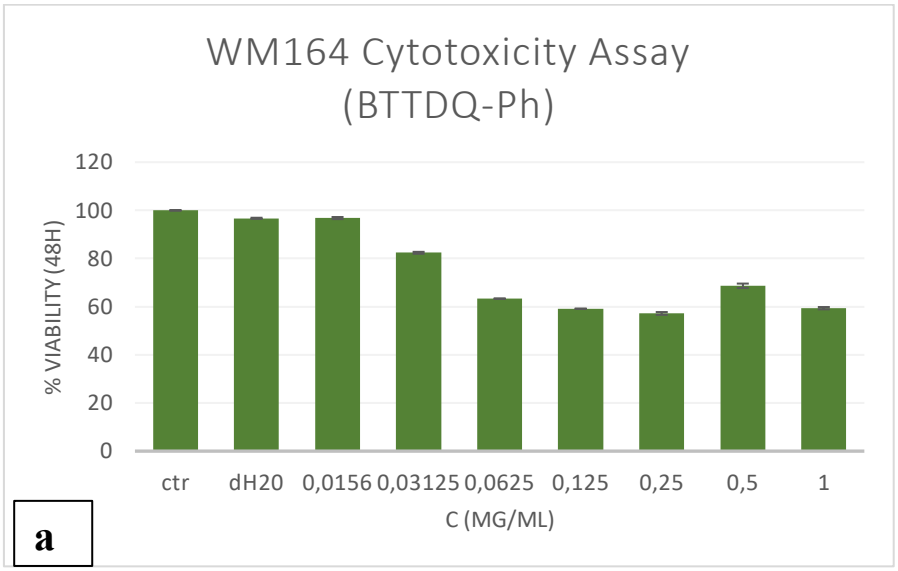

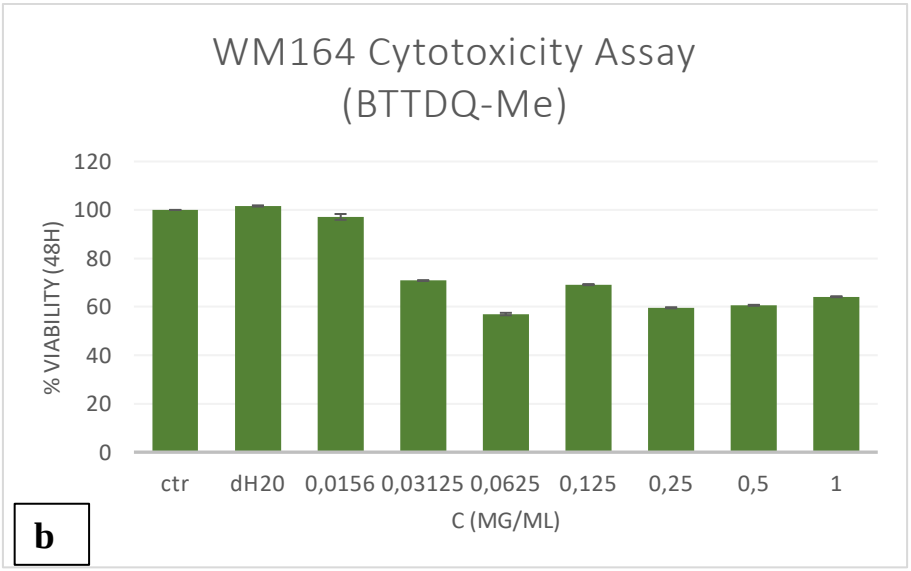

Fig. 23: Viability assay of WM164 on BTTDQ-Ph (a) and BTTDQ-Me (b) NPs.

The cell metabolic activity results revealed that both BTTDQ-Ph and BTTDQ-Me NPs - labeled MSCs have similar cell number with the NPs-free MSCs after 2 days of incubation. Specifically, WJ-MSC cells showed adhesion and even proliferation in several concentrates of both BTTDQ-Ph and BTTDQ-Me NPs [84],[85]. Apparently, the phenyl-substituted CPNs are considered as preferable to the viability WJ-MSC cells, since they exhibit lower levels of

cytotoxicity. According to fig. 21(a), the viability and proliferation of the cells labeled with the methyl-substituted CPNs, maintains an adequate level up until the concentration of 0.125 μg/mL. Comparatively, according to fig. 21(b) the BTTDQ-Ph NPs successfully reached higher folds of viability. More specifically, the triplicates of the following concentrations (*0.0315, 0.0156, 0.0625, 0.125, 0.25* and *0.5* μg/ml) exhibit the same or even higher levels of viability compared to the TCPS control ones [85]-[87]. On the other hand, the BTTDQ-Me NPs also exhibit a good viability and a subsequent low cytotoxicity, however, only in lower concentrations. As it is depicted in fig. 21(a,b) normal WJ-MSC cells interact well with the CPNs leading to high levels of viability, which confirms our initial assumption, that CP dots display low cytotoxicity levels on normal cells and are considered as biocompatible. In addition, the biocompatibility of CP nanoparticles, was also established by recent reports [86],[87]. The results of our cytotoxicity tests confirmed this statement since we observed a positive impact on cell growth. As it was observed, the cellular response is enhanced in terms of adhesion and proliferation of WJ-MSC in the presence of CP dots.

The viability assay of both WM164 human melanoma (Fig.22(a,b)) and HCT116 colon colorectal cancer cells (Fig.23(a,b)) on BTTDQ-Ph and BTTDQ-Me NPs was performed under the same conditions with the WJ-MSC cells. Cell viability was expressed by the ratio of the absorbance of MTS in the sample wells, to that of the cells incubated with culture medium only. Interestingly, in this cytotoxicity assay the melanoma and colorectal cancer cells-NPs interactions led to higher levels of cytotoxicity, compared to the normal WJ-MSC cells. Specifically, a notable 20-30% decrease in the viability of cancer cell lines is observed in the colon colorectal cancer cells, whereas the percentage of the cytotoxicity doubles with reference to the WM164 cell line. It is established that the mesenchymal cells are harder to be handled since they are more sensitive to contaminations, whereas cancer cells are considered as more durable. Subsequently, these results were a paradox since the NPs were not loaded with an anticancer drug. The chemical interactions between the biomaterial and the cells play a crucial role in the viability and proliferation of the cells. Consequently, the anticancer properties of the CPNs have to be investigated. Surprisingly, resent studies came up with comparable results, reinforcing our data [88]-[95]. In fact,

quinoxaline itself and also thiadiazole derivatives that used in the polymerization of the present study, display anticancer properties since they appear to be harmful for the cancer lines but beneficial for the mesenchymal cells with no profound side effect on their growth [88]-[95],[98]-[102]. Specifically, the latter literature reveals an anticancer mechanism of thiadiazole-derivatives and quinoxaline, that is not cytotoxic to directly damage the cancer cells, but induces their apoptosis at a certain time of cell division cycle [105].

4. Conclusion

Conjugated polymer nanoparticles are attractive bioimaging probes due to their excellent optical characteristics and low cytotoxicity. According to literature, a whole range of conjugated polymer particles have been synthesized up to now, with particle sizes ranging from the nano- to the micrometer scale and colors covering the entire visible range. It is of great importance, that the recent advances in synthetic procedures enable preparation of CPNs nanoparticles with narrow size distribution and well-controlled size, supporting their scale of reproducibility.

In conclusion, fluorescent materials namely BTTDQ-Ph and BTTDQ-Me were synthesized *via* Stille coupling. Herein, the spectral and colloidal properties of CPdots prepared by nanoprecipitation are reported. The low-bandgap CPdots exhibit absorption and emission maxima in the red or far-red spectral region. Specifically, the BTTDQ-Ph NPs absorbs at 660 nm and emits at 745 nm, whereas the BTTDQ-Me NPs absorbs at 580 nm and emits at 745, respectively. Apart from their spectral properties, their colloidal ones were also examined. The results from the zeta potential assessment indicate that in the terms of our three-week study, the NPs exhibit colloidal stability with a zeta potential of approximately -20 mV. Moreover, DLS, TEM and FESEM analyses revealed that the average size of the NPs is lower than 100 nm, an ideal size for bio-applications [1],[104],[105]. The cytotoxicity analysis confirmed the biocompatibility of the water-soluble NPs to the WJ-MSC cells and highlighted their anticancer potential regarding the viability of WM164 and HCT116 cell lines, supporting their potential use not only as low-bandgap fluorescent probes for bio-

imaging in several cancer types, but also in their subsequent therapy.

Overall, based on the steady improvements reported in literature on the brightness, stability, cell viability and theranostic nature of many conjugated polymer nanoparticles, a 'bright ' future is ahead for the bioimaging of conjugated polymer nanoparticles that will introduce a new generation of fluorescent probes that appear to be the quintessential contrast agents.

5. References

[1]. Erratum: 2-Hydroxy-3-methoxybenzoic acid attenuates mast cell-mediated allergic reaction in mice via modulation of the FcεRI signaling pathway. (2017). *Acta Pharmacologica Sinica, 38(3), 444–444.* doi:10.1038/aps.2017.4

[2]. Feng, L., Zhu, C., Yuan, H., Liu, L., Lv, F., & Wang, S. (2013). Conjugated polymer nanoparticles: preparation, properties, functionalization and biological applications. Chemical Society Reviews, 42(16), 6620.doi:10.1039/c3cs60036j

[3]. V. Rohatgi, Low-Bandgap Conjugated Polymer Dots for Near-Infrared Fluorescence Imaging.,ACS Appl. Nano Mater., 2018, 1 (9), pp 4801–4808 DOI: 10.1021/acsanm.8b01014

[4]. Zhu, C.; Liu, L.; Yang, Q.; Lv, F.; Wang, S. Water-Soluble Conjugated Polymers for Imaging, Diagnosis, and Therapy. Chem. Rev. 2012, 112, 4687-4735

[5]. Wu, C. & Chiu, D. T. Highly fluorescent semiconducting polymer dots for biology and medicine. Angew. Chem. Int. Ed. 52, 3086–3109 (2013).

[6]. Siegel, R. L., Miller, K. D., & Jemal, A. (2019). *Cancer statistics, 2019. CA: A Cancer*

Journal for Clinicians, 69(1), 7–34. doi:10.3322/caac.21551

[7]. Ferlay J, Soerjomataram I, Ervik M, Dikshit R, Eser S, Mathers C et al. GLOBOCAN 2012 v1.0, Cancer Incidence and Mortality Worldwide: IARC CancerBase No. 11 Lyon, France: International Agency for Research on Cancer; 2013.

[8]. GBD 2015 Risk Factors Collaborators. Global, regional, and national comparative risk assessment of 79 behavioural, environmental and occupational, and metabolic risks or clusters of risks, 1990-2015: a systematic analysis for the Global Burden of Disease Study 2015. Lancet. 2016 Oct; 388 (10053):1659-1724.

[9]. Plummer M, de Martel C, Vignat J, Ferlay J, Bray F, Franceschi S. Global burden of cancers attributable to infections in 2012: a synthetic analysis. Lancet Glob Health. 2016 Sep;4(9):e609-16. doi: 10.1016/S2214-109X(16)30143-7.

[10]. Stewart BW, Wild CP, editors. World cancer report 2014 Lyon: International Agency for Research on Cancer; 2014.

[11]. Global Initiative for Cancer Registry Development. International Agency for Research on Cancer, Lyon: France.

[12]. Hawkes, N. (2019). *Cancer survival data emphasise importance of early diagnosis. BMJ, l408.* doi:10.1136/bmj.l408

[13]. Glunde K, Pathak A, Bhujwalla Z. Molecular-functional imaging of cancer: to image and imagine. Trends Mol. Med. 2007;13(7):287–29

[14]. Hanahan D, Weinberg RA. The hallmarks of cancer. Cell. 2000;100(1):57–70.

[15]. Hong WK, Sporn MB. Recent advances in chemoprevention of cancer. Science. 1997;278(5340):1073–1077.

[16]. Pomper MG. Molecular imaging: an overview. Acad. Radiol. 2001;8(11):1141–1153.

[17]. Moore SG, Shenoy PJ, Fanucchi L, Tumeh JW, Flowers CR. Cost–effectiveness of MRI

compared with mammography for breast cancer screening in a high-risk population. BMC Health Serv. Res. 2009;9:9.

[18]. Advances in molecular imaging: targeted optical contrast agents for cancer diagnostics, Nanomedicine (Lond). 2012 Mar; 7(3): 429–445., doi:10.2217/nnm.12.12, Anne Hellebust and Rebecca Richards-Kortum

[19]. Mahendra Rai, Aniket Gade, Swapnil Gaikwad, Priscyla D. Marcato and Nelson Durán, J. Braz. Chem. Soc., 23, (2012), 14-24.

[20]. Dede S. and Altay F., Biosensors from the First Generation to Nano-biosensors, Int. Adv. Res. Eng. J., 02, (2018), 200-207.

[21]. Harun, M.H.; Saion, E.; Kassim, A.; Yahya, N.; Mahmud, E. Conjugated conducting polymers: A brief overview. UCSI Acad. J. J. Adv. Sci. Arts 2007, 2, 63–68.

[22]. Conjugated Polymers: Theory, Synthesis, Properties, and Characterization (Handbook of Conducting Polymers, Fourth Edition), CRC Press 2007, Taylor & Francis Group, LLC.

[23]. Zare, E. N., Lakouraj, M. M., & Ashna, A. (2018). Synthesis of conductive poly (3-aminobenzoic acid) nanostructures with different shapes in acidic ionic liquids medium. Journal of Molecular Liquids, 271, 514–521. doi:10.1016/j.molliq.2018.09.028.

[24]. Pavase, T. R., Lin, H., Shaikh, Q., Hussain, S., Li, Z., Ahmed, I., Kalhoro, M. T. (2018). Recent advances of conjugated polymer (CP) nanocomposite-based chemical sensors and their applications in food spoilage detection: A comprehensive review. Sensors and Actuators B: Chemical, 273, 1113–1138. doi:10.1016/j.snb.2018.06.118.

[25]. W. Locke and the ICSTM Department of Chemistry 1996-97.

[27]. Huo, L., Chen, H.-Y., Hou, J., Chen, T. L. & Yang, Y. Low band gap dithieno[3,2-b:2 ‘,3 ‘-d]silole-containing polymers, synthesis, characterization and photovoltaic application. Chem. Commun. 5570-5572 (2009).

[28]. Hashemi, D., Ma, X., Ansari, R., Kim, J., & Kieffer, J. (2019). Design principles for the energy level tuning in donor/acceptor conjugated polymers. Physical Chemistry Chemical Physics, 21(2), 789–799. doi:10.1039/c8cp03341b

[29]. Guenes, S., Neugebauer, H., & Sariciftci, N. S. (2007). Conjugated Polymer-Based Organic Solar Cells. ChemInform, 38(31). doi:10.1002/chin.200731220

[30]. Abdullah A. Hussein,Abdullwahab A. Sultan,Mohammed T. Obeid Asheaq T. Abdulnabi and Mohammed T. Ali, Synthesis and Characterization of poly(3-hexylthiophene).International Journal of Scientific Engineering and Applied Science (IJSEAS) -Volume-1, Issue-7,October2015ISSN: 2395-3470.

[31]. Qian, C., Chen, Y., Feng, P., Xiao, X., Dong, M., Yu, J., Gu, Z. (2017). Conjugated polymer nanomaterials for theranostics. Acta Pharmacologica Sinica, 38(6), 764–781. doi:10.1038/aps.2017.42

[32]. Fundamentals of Conjugated Polymer Blends, Copolymers and Composites. Copyright 2015 by Scrivener Publishing LLC.

[33]. Davies, A. M. C. (2005). An Introduction to near Infrared Spectroscopy. NIR News, 16(7), 9–11. doi:10.1255/nirn.853.

[34]. Miyaura, N. and Suzuki, A. (1995) Palladium-catalyzed cross-coupling reactions oforganoboron compounds.Chem. Rev.,95, 2457–2483.

[35]. Beletskaya, I.P. and Cheprakov, A.V. (2000) The Heck reaction as a sharpening stone of palladium catalysis.Chem. Rev.,100, 3009–3066.

[36]. Corbet, J.-P. and Mignani, G. (2006) Selected patented cross-coupling reactiontechnologies.Chem. Rev.,106, 2651–2710.

[37]. Carsten, B., He, F., Son, H.J., Xu, T., and Yu, L. (2011) Stille polycondensation for synthesis of functional materials.Chem. Rev.,111, 1493–1528.

[38]. Feg, L., Zhu, C., Yuan, H. et al. (2013) Conjugated polymer nanoparticles: preparation, properties, functionalization and biological applications, Chem. Soc. Rev., 42, 6620-6633.

[39]. Tuncel, D., and Demir, H.V. (2010) Conjugated polymers nanoparticles, Nanoscale, 2, 484-494.

[40]. Burroughes, J.H., Bradley, D.D.C., Brown, A.R. et al. (1990) Light-emitting diodes based on conjugated polymers. Nature, 347, 539-541.

[41]. Hide, F., Diaz-Garcia, M., and Schwarty, B. (1996) Semiconducting polymers: a new class of solid-state laser materials. Science, 273, 1833-1836.

[42]. Zhu C, Liu L, Yang Q, Lv F, Wang S., Water-soluble conjugated polymers for imaging, diagnosis, and therapy. Chem Rev. 2012 Aug 8;112(8):4687-735. doi: 10.1021/cr200263w.

[43]. Dash, B.C., Rethore, G., Monaghan, M. et al. (2010) The influence of size and charge of chitosan/polyglutamic acid hollow spheres on cellular internalization, viability and blood compatibility. Biomaterials, 31, 8188-8197.

[44]. Florez, L., Herrmann, C., Cramer, J.M. et al. (2012) How shape influences uptake: interactions of anisotropic polymer nanoparticles and human mesenchymal stem cell. Small, 8, 2222-2230

[45]. Szymanski C, Wu C, Hooper J, Salazar MA, Perdomo A, Dukes A, McNeill J, Single molecule nanoparticles of the conjugated polymer MEH-PPV, preparation and characterization by near-field scanning optical microscopy.J Phys Chem B. 2005 May 12;109(18):8543-6, DOI: 10.1021/jp051062k .

[46]. Hitoshi Kasai, Hirokazu Kamatani, Shuji Okada, Hidetoshi Oikawa, Hiro Matsuda[1] and Hachiro Nakanishi, Size-Dependent Colors and Luminescences of Organic Microcrystals. *Jpn. J. Appl. Phys.* **35** L221, https://doi.org/10.1143/JJAP.35.L221

[47]. Haken, J. K. (1992). Modern methods of polymer characterization. Journal of Chromatography A, 606(2), 297–298. doi:10.1016/0021-9673(92)87042-7

[48]. Binder, W. H., & Sachsenhofer, R. (2007). “Click” Chemistry in Polymer and Materials Science. Macromolecular Rapid Communications, 28(1), 15–54. doi:10.1002/marc.200600625

[49]. H.-H. Perkampus, UV-VIS Spectroscopy and Its Applications, DOI:10.1007/978-3-642-77479-9, Chapter 1-3.

[50]. Fultz, B & Howe, J (2007). Transmission Electron Microscopy and Diffractometry of Materials. Springer. ISBN 978-3-540-73885-5.

[51]. Egerton, R (2005). Physical principles of electron microscopy. Springer. ISBN 978-0-387-25800-3.

[52]. Rose, H H (2008). "Optics of high-performance electron Microscopes". Science and Technology of Advanced Materials. **9** (1): 014107. doi:10.1088/0031-8949/9/1/014107.

[53]. ISO 22412:2017. Particle Size Analysis – Dynamic Light Scattering (DLS). International Organization for Standardization.

[54]. Anton Paar. (n.d.) Faster, More Sensitive Zeta-Potential Measurements with cmPALS and the Litesizer™500.[January,24,2019].

[55]. Bellmann, C., Caspari, A., Moitzi, C., Fradler, C., Babick, F. (2018) DLS & ELS Guide.

[56]. Y. Hong, J. W. Y. Lam, and B. Z. Tang, Chem. Commun., 2009, 4332.

[57]. M. Anpo, M. Kondo, S. Coluccia, C. Louis, and M. Che, J. Am. Chem. Soc., 1989, 111, 8791.

[58]. N. S. Sariciftci, Primary Photoexcitations In Conjugated Polymers Molecular Exciton Versus Semiconductor Band Model, World Scientific Publishing Company, Singapore (1997).

[59]. D. C. Harris, Quantitative Chemical Analysis, 7th Ed, W. H. Freeman and Company,

New York (2006).

[60]. Wang, H.-S., Hung, S.-C., Peng, S.-T., Huang, C.-C., Wei, H.-M., Guo, Y.-J., Chen, C.-C. (2004). Mesenchymal Stem Cells in the Wharton's Jelly of the Human Umbilical Cord. Stem Cells, 22(7), 1330–1337. doi:10.1634/stemcells.2004-0013

[61]. Zhu, Pengxi (11 February 2016). "Inhibition of Growth and Metastasis of Colon Cancer by Delivering 5-Fluorouracil-loaded Pluronic P85 Copolymer Micelles". Scientific Reports. **6**. doi:10.1038/srep20896

[62]. Rajput, Ashwani; et al. (15 June 2008). "Characterization of HCT116 Human Colon Cancer Cells in an Orthotopic Model". Journal of Surgical Research. **147** (2): 276–281. doi:10.1016/j.jss.2007.04.021. PMID17961596

[63]. Paraiso, K. H. T., Fedorenko, I. V., Cantini, L. P., Munko, A. C., Hall, M., Sondak, V. K., Smalley, K. S. M. (2010). Recovery of phospho-ERK activity allows melanoma cells to escape from BRAF inhibitor therapy. British Journal of Cancer, 102(12), 1724–1730. doi:10.1038/sj.bjc.6605714

[64]. Troyer, D. L., & Weiss, M. L. (2008). Concise Review: Wharton's Jelly-Derived Cells Are a Primitive Stromal Cell Population. Stem Cells, 26(3), 591–599. doi:10.1634/stemcells.2007-0439.

[65]. Feng, L., Zhu, C., Yuan, H., Liu, L., Lv, F., & Wang, S. (2013). *Conjugated polymer nanoparticles: preparation, properties, functionalization and biological applications. Chemical Society Reviews, 42(16), 6620.* doi:10.1039/c3cs60036j

[66]. Szymanski, C.; Wu, C.; Hooper, J.; Salazar, M.A.; Perdomo, A.; Dukes, A.; McNeill, J. Single MoleculeNanoparticles of the Conjugated Polymer MEH-PPV, Preparation and Characterization by Near-FieldScanning Optical Microscopy.J. Phys. Chem. B2005,109, 8543–8546

[67]. Wu, C.; Peng, H.; Jiang, Y.; McNeill, C. Energy Transfer Mediated Fluorescence from Blended ConjugatedPolymer Nanoparticles.J. Phys. Chem. B2006,110, 14148–14154

[68]. Braeken, Y., Cheruku, S., Ethirajan, A., & Maes, W. (2017). *Conjugated Polymer Nanoparticles for Bioimaging. Materials, 10(12), 1420.* doi:10.3390/ma10121420.

[69]. Li, K., Pan, J., Feng, S.-S., Wu, A. W., Pu, K.-Y., Liu, Y., & Liu, B. (2009). *Generic Strategy of Preparing Fluorescent Conjugated-Polymer-Loaded Poly(DL-lactide-co-Glycolide) Nanoparticles for Targeted Cell Imaging. Advanced Functional Materials, 19(22), 3535–3542.* doi:10.1002/adfm.200901098.

[70]. H. J. Dou, M. Jiang, H. S. Peng, D. Y. Chen, Y. Hong,Angew. Chem. Int. Ed.2003,42, 1516.

[71]. H. W. Tang, C. F. Xing, L. B. Liu, Q. Yang and S. Wang,Small, 2011,7, 1464–1470.

[72]. Ahmed, E., Morton, S. W., Hammond, P. T., & Swager, T. M. (2013). Fluorescent Multiblock π-Conjugated Polymer Nanoparticles for In Vivo Tumor Targeting. Advanced Materials, 25(32), 4504–4510. doi:10.1002/adma.201301656.

[73]. Li, K., & Liu, B. (2012). Polymer encapsulated conjugated polymernanoparticles for fluorescence bioimaging. J. Mater. Chem., 22(4), 1257–1264. doi:10.1039/c1jm14397b.

[74]. Li, K., Ding, D., Huo, D., Pu, K.-Y., Thao, N. N. P., Hu, Y., Liu, B. (2012). Conjugated Polymer Based Nanoparticles as Dual-Modal Probes for Targeted In Vivo Fluorescence and Magnetic Resonance Imaging. Advanced Functional Materials, 22(15), 3107–3115. doi:10.1002/adfm.201102234.

[75]. Aldakov, D., Palacios, M. A., & Anzenbacher, P. (2005). Benzothiadiazoles and Dipyrrolyl Quinoxalines with Extended Conjugated Chromophores−Fluorophores and Anion Sensors. Chemistry of Materials, 17(21), 5238–5241. doi:10.1021/cm050985p

[76]. Chappell, J., Lidzey, D. G., Jukes, P. C., Higgins, A. M., Thompson, R. L., O'Connor, S., Jones, R. A. L. (2003). Correlating structure with fluorescence emission in phase-separated conjugated-polymer blends. Nature Materials, 2(9), 616–621. doi:10.1038/nmat959.

[77]. Kato, S., Matsumoto, T., Ishi-i, T., Thiemann, T., Shigeiwa, M., Gorohmaru, H., …

Mataka, S. (2004). Strongly red-fluorescent novel donor–π-bridge–acceptor–π-bridge–donor (D–π–A–π–D) type 2,1,3-benzothiadiazoles with enhanced two-photon absorption cross-sections. Chem. Commun., (20), 2342–2343. doi:10.1039/b410016f .

[78]. Justin Thomas, K. R., Lin, J. T., Velusamy, M., Tao, Y.-T., & Chuen, C.-H. (2004). Color Tuning in Benzo[1,2,5]thiadiazole-Based Small Molecules by Amino Conjugation/Deconjugation: Bright Red-Light-Emitting Diodes. Advanced Functional Materials, 14(1), 83–90. doi:10.1002/adfm.200304486.

[79]. H. Raveendranatha Reddya, S. Jayakumarb, R.Subashini, The synthesis and Photophysical studies of Quinoxaline derivatives-Synthesis of Quinoxalines as Cu (II) and Pb (II) ion fluorescent sensors, IJFST (2015), Volume3, p;129-135.

[80]. Blanco, E., Shen, H., & Ferrari, M. (2015). Principles of nanoparticle design for overcoming biological barriers to drug delivery. Nature Biotechnology, 33(9), 941–951. doi:10.1038/nbt.3330

[81]. David Putnam, Christine A. Gentry, Daniel W. Pack, and Robert Langer, Polymer-based gene delivery with low cytotoxicity by a unique balance of side-chain termini, PNAS January 30, 2001 98 (3) 1200-1205; https://doi.org/10.1073/pnas.98.3.1200

[82]. Padmaparna Chaudhuri, Abhimanyu Paraskar⊥, Shivani Soni⊥, Raghunath A. Mashelkar, Shiladitya Sengupta,Fullerenol−Cytotoxic Conjugates for Cancer Chemotherapy, *ACS Nano*2009392505-2514, Publication Date:August 14, 2009, https://doi.org/10.1021/nn900318y

[83]. Chunlei Zhu, Libing Liu, Qiong Yang, Fengting Lv, Shu Wang**,** Water-Soluble Conjugated Polymers for Imaging, Diagnosis, and Therapy, Chem. Rev.201211284687-4735, Publication Date: June 6, 2012, https://doi.org/10.1021/cr200263w.

[84]. Guo, B., Sheng, Z., Kenry, K., Hu, D., Lin, X., Xu, S., Liu, B. (2017). Biocompatible conjugated polymer nanoparticles for highly efficient photoacoustic imaging of orthotopic brain tumors in the second near-infrared window. Mater. Horiz., 4(6), 1151–1156.

doi:10.1039/c7mh00672a.

[85]. Geng, J., Sun, C., Liu, J., Liao, L.-D., Yuan, Y., Thakor, N., Liu, B. (2014). Biocompatible Conjugated Polymer Nanoparticles for Efficient Photothermal Tumor Therapy. Small, 11(13), 1603–1610. doi:10.1002/smll.201402092.

[86]. Li, K., & Liu, B. (2012). Polymer encapsulated conjugated polymernanoparticles for fluorescence bioimaging. J. Mater. Chem., 22(4), 1257–1264. doi:10.1039/c1jm14397b

[87]. Ding, D., Li, K., Zhu, Z., Pu, K.-Y., Hu, Y., Jiang, X., & Liu, B. (2011). Conjugated polyelectrolyte–cisplatin complex nanoparticles for simultaneous in vivo imaging and drug tracking. Nanoscale, 3(5), 1997. doi:10.1039/c0nr00950d

[88]. Jin, G., Mao, D., Cai, P., Liu, R., Tomczak, N., Liu, J., Li, K. (2015). Conjugated Polymer Nanodots as Ultrastable Long-Term Trackers to Understand Mesenchymal Stem Cell Therapy in Skin Regeneration. Advanced Functional Materials, 25(27), 4263–4273. doi:10.1002/adfm.201501081.

[89]. Pires, F., Ferreira, Q., Rodrigues, C. A. V., Morgado, J., & Ferreira, F. C. (2015). Neural stem cell differentiation by electrical stimulation using a cross-linked PEDOT substrate: Expanding the use of biocompatible conjugated conductive polymers for neural tissue engineering. Biochimica et Biophysica Acta (BBA) - General Subjects, 1850(6), 1158–1168. doi:10.1016/j.bbagen.2015.01.020.

[90]. Ningegowda, R., Shivananju, N. S., Rajendran, P., Basappa, Rangappa, K. S., Chinnathambi, A., Priya, B. S. (2016). A novel 4,6-disubstituted-1,2,4-triazolo-1,3,4-thiadiazole derivative inhibits tumor cell invasion and potentiates the apoptotic effect of TNFα by abrogating NF-κB activation cascade. Apoptosis, 22(1), 145–157. doi:10.1007/s10495-016-1312-8

[91]. Rashdan, H. R. M., Farag, M. M., El-Gendey, M. S., & Mounier, M. M. (2019). Toward Rational Design of Novel Anti-Cancer Drugs Based on Targeting, Solubility, and Bioavailability Exemplified by 1,3,4-Thiadiazole Derivatives Synthesized Under Solvent-

Free Conditions. Molecules, 24(13), 2371. doi:10.3390/molecules24132371.

[92]. Gomha, S., Edrees, M., Muhammad, Z., & El-Reedy, A. (2018). 5-(Thiophen-2-yl)-1,3,4-thiadiazole derivatives: synthesis, molecular docking and *in vitro* cytotoxicity evaluation as potential anticancer agents. Drug Design, Development and Therapy, Volume 12, 1511–1523. doi:10.2147/dddt.s165276.

[93]**.** Altıntop, Mehlika D.; Sever, Belgin; Özdemir, Ahmet; Ilgın, Sinem; Atlı, Özlem; Turan-Zitouni, Gülhan; Kaplancıklı, Zafer A.,Anti-Cancer Agents in Medicinal Chemistry (Formerly Current Medicinal Chemistry - Anti-Cancer Agents), Volume 18, Number 11, 2018, pp. 1606-1616(11). Synthesis and Evaluation of a Series of 1,3,4-Thiadiazole Derivatives as Potential Anticancer Agents, https://doi.org/10.2174/1871520618666180509111351

[94]. Özdemir, A., Sever, B., Altıntop, M., Temel, H., Atlı, Ö., Baysal, M., & Demirci, F. (2017). Synthesis and Evaluation of New Oxadiazole, Thiadiazole, and Triazole Derivatives as Potential Anticancer Agents Targeting MMP-9. Molecules, 22(7), 1109. doi:10.3390/molecules22071109.

[95]. Han, Y. T., Jung, J.-W., & Kim, N.-J. (2017). Recent Advances in the Synthesis of Biologically Active Cinnoline, Phthalazine and Quinoxaline Derivatives. Current Organic Chemistry, 21(14), 1265–1291. doi:10.2174/1385272821666170221150 9.

[96]. Rajule, R., Bryant, V. C., Lopez, H., Luo, X., & Natarajan, A. (2012). Perturbing pro-survival proteins using quinoxaline derivatives: A structure–activity relationship study. Bioorganic & Medicinal Chemistry, 20(7), 2227–2234. doi:10.1016/j.bmc.2012.02.022.

[97]. Gowramma, Byran; Praveen, Thaggikuppe K.;Gomathy, Subramanian; Kalirajan, Rajagopal; Babu, Baswan;Krishnavenic, Nagappan, Current Bioactive Compounds, Volume 14, Number 3, 2018, pp. 309-316(8) Synthesis of 2-(Bis (2-Chloroethyl)Amino)-N-(5-Substitutedphenyl)- 1,3,4-Thiadiazol-2-Yl)Acetohydrazide And Evaluation of Anticancer Activity. https://doi.org/10.2174/1573407213666170428110528

[98]. Montana, M., Mathias, F., Terme, T., & Vanelle, P. (2018). Antitumoral activity of

quinoxaline derivatives: A systematic review. European Journal of Medicinal Chemistry. doi:10.1016/j.ejmech.2018.11.059

[99]. Feng, Q., & Tong, R. (2016). Anticancer nanoparticulate polymer-drug conjugate. Bioengineering & Translational Medicine, 1(3), 277–296. doi:10.1002/btm2.10033.

[100]. Kaushal, T., Srivastava, G., Sharma, A., & Negi, A. S. (2018). An Insight into Medicinal Chemistry of Anticancer Quinoxalines. Bioorganic & Medicinal Chemistry. doi:10.1016/j.bmc.2018.11.021

[101]. Lee, S.-H., Kim, N., Kim, S.-J., Song, J., Gong, Y.-D., & Kim, S.-Y. (2013). Anti-cancer effect of a quinoxaline derivative GK13 as a transglutaminase 2 inhibitor. Journal of Cancer Research and Clinical Oncology, 139(8), 1279–1294. doi:10.1007/s00432-013-1433-1.

[102]. Aliya M. S. E Newahie1, Yassin M. Nissan, Nasser S. M. Ismail, Dalal A. Abou E Ella, Sohair M. Khojah and Khaled A.M. Abouzid, Design and Synthesis of New QuinoxalineDerivatives as Anticancer Agents and Apoptotic Inducers, *Molecules* **2019**, *24*(6), 1175; https://doi.org/10.3390/molecules24061175

[103]. Liu, L., Yu, M., Duan, X., & Wang, S. (2010). Conjugated polymers as multifunctional biomedical platforms: Anticancer activity and apoptosis imaging. Journal of Materials Chemistry, 20(33), 6942. doi:10.1039/c0jm01078b.

[104]. Dandan Chen, I-Che Wu, Zhihe Liu, Ying Tang, Haobin Chen, Jiangbo Yu, Changfeng Wu and Daniel T. Chiu, Semiconducting polymer dots with bright narrow band emission at 800 nm for biological applications, Chem. Sci., 2017, 8, 3390

[105]. Braeken, Y., Cheruku, S., Ethirajan, A., & Maes, W. (2017). Conjugated Polymer Nanoparticles for Bioimaging. Materials, 10(12), 1420. doi:10.3390/ma10121420.